CHARACTERIZATION OF STRESS IN GAN-ON-SAPPHIRE
MICROELECTROMECHANICAL SYSTEMS (MEMS) STRUCTURES
USING MICRO-RAMAN SPECTROSCOPY

THESIS

Francisco E. Parada, First Lieutenant, USAF

AFIT/GEO/ENP/06-02

DEPARTMENT OF THE AIR FORCE
AIR UNIVERSITY

AIR FORCE INSTITUTE OF TECHNOLOGY

Wright-Patterson Air Force Base, Ohio

Characterization of Stress in GaN-on-Sapphire Microelectromechanical Systems (MEMS) Structures Using Micro-Raman Spectroscopy

THESIS

Presented to the Faculty

Department of Engineering Physics

Graduate School of Engineering and Management

Air Force Institute of Technology

Air University

Air Education and Training Command

In Partial Fulfillment of the Requirements for the

Degree of Master of Science in Electrical Engineering

Francisco E. Parada, B.S.E.E.

First Lieutenant, USAF

March 2006

AFIT/GEO/ENP/06-02

Characterization of Stress in GaN-on-Sapphire Microelectromechanical Systems (MEMS) Structures Using Micro-Raman Spectroscopy

Francisco E. Parada, B.S.E.E.

First Lieutenant, USAF

Approved:

/signed/		13 Mar 2006
Michael A. Marciniak (Chairman)		date
/signed/		13 Mar 2006
LaVern A. Starman (Member)		date
/signed/		13 Mar 2006
Jason Foley (Member)		date

Abstract

Micro-Raman (μRaman) spectroscopy is an efficient, non-destructive technique widely used to determine the quality of semiconductor materials and microelectrome-chanical systems. This work characterizes the stress distribution in wurtzite gallium nitride grown on c-plane sapphire substrates by molecular beam epitaxy. This wide bandgap semiconductor material is being considered by the Air Force Research Laboratory for the fabrication of shock-hardened MEMS accelerometers. μRaman spectroscopy is particularly useful for stress characterization because of its ability to measure the spectral shifts in Raman peaks in a material, and correlate those shifts to stress and strain. The spectral peak shift as a function of stress, known as the phonon deformation potential, is determined by applying strain to the material using a four-point strain fixture while simultaneously monitoring the applied strain and recording the Raman spectrum. The deformation potentials are then used to determine stress distribution; the spectral positions of the E_2 Raman mode ($\nu = 569\ cm^{-1}$) in GaN and A_{1g} Raman mode ($\nu = 418\ cm^{-1}$) in sapphire are recorded at each spatial position in a raster map. The μRaman spectroscopy is performed using a Renishaw InVia Raman spectrometer with argon ion ($\lambda = 514.5\ nm$, $h\nu = 2.41eV$) and helium-neon ($\lambda = 633\ nm$, $h\nu = 1.96\ eV$) excitation sources, and the data is collected across the samples with 5- to 10-μm spatial resolution. Inherent stress and evidence of significant damage in the GaN layer due to MEMS processing is discussed.

Acknowledgements

I would like to extend my sincere thanks to Dr. Michael Marciniak and my other committee members, Maj LaVern Starman and Jason Foley. Their remarkable knowledge and expertise guided me throughout the research effort. Also, I would like thank Mr. David Liptak, Dr. Joe Van Nostrand, Mr. Larry Callahan, Dr. David Tomich, and Ms. Becky Cortez from AFRL for their valuable and timely input. My family has been instrumental througout this process and I will be forever be grateful for their support, understanding, and love.

Francisco E. Parada

Table of Contents

vi

List of Figures

List of Tables

List of Abbreviations

Characterization of Stress in GaN-on-Sapphire Microelectromechanical Systems (MEMS) Structures Using Micro-Raman Spectroscopy

I. Introduction

The motivation for this research lies primarily in today's battlefield, and the need to design and fabricate systems able to withstand the harsh conditions our military encounters. The Munitions Directorate of the Air Force Research Laboratory (AFRL/MN), Air Force Materiel Command (AFMC), in collaboration with the National Aeronautic Space Administration's (NASA) Glenn Research Center, Air Force Institute of Technology (AFIT) and others, is pursuing the development of hardened inertial sensors for use in penetrating weapons. Micropressure sensors are a type of microelectromechanical systems (MEMS)that function on the principle of mechanical deformation (*i.e.*, deflection) and stresses of thin membranes.

MEMS are relatively a new technology which combine electrical and mechanical functions at the micrometer (μm) scale. Most of the research has concentrated on developing new fabrication techniques and showing their potential. Over the past few years, great progress has been made in the area of MEMS, but a limiting factor is often material selection. Based solely on their size, these devices can be made to provide better sensitivities or responses to various inputs. Formally, the most salient characteristics of MEMS are: (1) The microfabrication process used to make the devices should be scaleable. This is obviously important because of production. It has to be realizable at low cost. (2) There is some level of integration, which refers to coupling electronic and non-electronic functions [18].

1.1 Problem Statement and Research Objectives

This research constitutes a continuing effort to characterize materials for the fabrication of inertial sensors. The main purpose is to determine the stress state

as a measure of the quality of gallium nitride (GaN) on c-plane sapphire circular membranes fabricated using a novel micromachining laser drilling process.

The research objectives are: 1) Model, using finite element analysis, the behavior of circular membranes; 2) Analyze the quality of the as-grown GaN on c-plane sapphire film using x-ray diffraction, Zygo interferometry, and surface profilometry; and 3) to determine the stress distribution in the fabricated circular membranes using micro-Raman (μRaman) spectroscopy. LaVern A. Starman, in his doctoral dissertation titled, "Characterization of Residual Stress in MEMS Devices using Raman Spectroscopy [19]," demonstrated that, using the nondestructive evaluation μRaman spectroscopy, one could map the stress profiles of MEMS devices. This research works follows his approach

1.2 Organization

This thesis is organized in four main chapters. Chapter II covers basic background information on MEMS devices in general, as well as micro-pressure sensors; it also discusses the importance of finite element analysis in arriving at optimized devices; the principles of micro-Raman spectroscopy are presented; and a brief introduction to x-ray diffraction is given. Chapter III provides an overview of the samples available for this research. Chapter IV provides a detailed account of the experimental procedures performed to meet the research objectives. The experimental results and analysis are presented in Chapter V. And finally, conclusions and recommendations for future work are covered in Chapter VI.

II. Background

This chapter discusses topics relevant to the characterization of GaN on c-plane sapphire. Section 2.1 discusses micropressure sensors as MEMS and the use of wide bandgap semiconductor (WBG) materials for their fabrication. Section 2.2 briefly covers finite element analysis and specifically describes the software suite, CoventorWare. Section 2.3 describes WBG materials and specifically addresses the properties of GaN grown on c-plane sapphire. Section 2.4 covers Raman spectroscopy and its application to determining the stress in semiconductor materials. A brief introduction to x-ray diffraction (XRD) is given in Section 2.5.

2.1 MEMS Micropressure Sensors

There are three ways to fabricate MEMS: surface micromachining, bulk micromachining, and molding. Surface micromachining is a process that has evolved directly from the complementary metal-oxide-semiconductor electronic fabrication processes. In this process, layers are patterned and etched. In order to obtain the different elements (electromechanical), sacrificial layers are released. In bulk micromachining, part of the substrate is etched away to yield the electromechanical elements. One significant difference between these two methods is that higher aspect elements can be achieved through bulk micromachining because there is no limitation in layer size. Devices can be larger and obviously deeper. Molding, the third method, is perhaps the most versatile of the three methods because it allows for a great number of materials that could possibly be used to fabricate the devices. Molding is the deposition of material into a microfabricated mold. The most common is the process known by its acronym LIGA, which stands for Lithography, Galvanoformung (electroforming), and Abformung (molding). The flexibility of this method, as pointed out above, could possibly be negated by the fact that integration would be difficult simply because the process is not CMOS compatible like bulk or surface micromachining.

Micropressure sensors are MEMS that have been around for decades. Strictly speaking, micropressure sensors are transducers in which the sensing mechanism re-

lies on the material's piezoresistivity, piezoelectricity, capacitance, or other properties. Figure 2.1 is a top view of a piezoresistive pressure sensor in which the major components are highlighted. The piezoresistive elements (elements 1-4) are essentially semiconductor strain gages, which produce a change of electrical resistance because of the induced mechanical stress in the sensor. These elements are arranged in a Wheatstone bridge configuration.
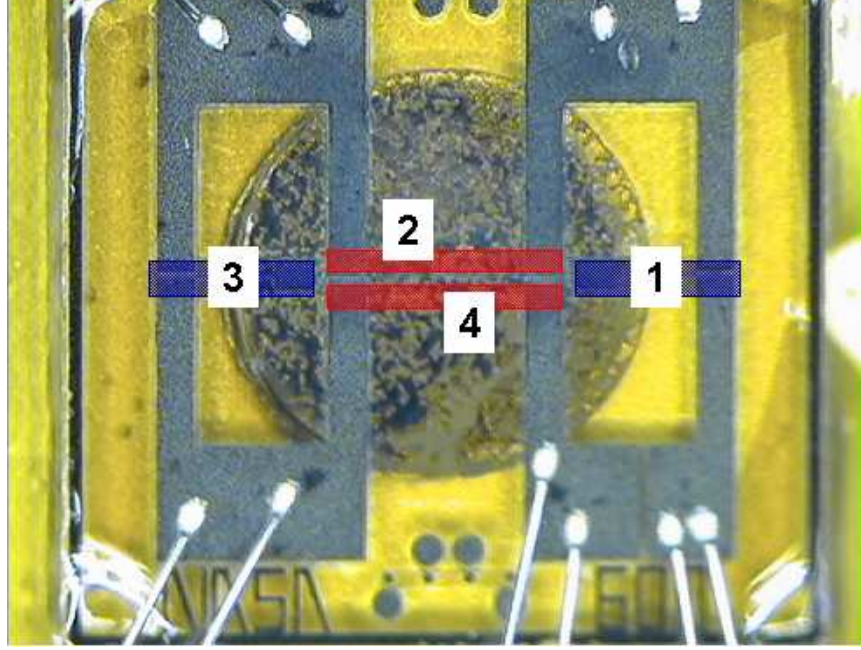
Figure 2.1:   6H-SiC pressure sensor showing the Wheatstone bridge configuration of the piezoresistive elements deposited on the diaphragm [11].

Transducers of this type can be fabricated using bulk or surface micromachining techniques. The primary advantage of using surface micromachining is that device features are usually smaller than in bulk micro-machined structures. Regardless, the planar nature of the fabrication process enables the designer to employ diaphragms as the main form of sensing element. Application of a uniform pressure on either side of the membrane results in deflection. Figure 2.2 shows the deflection of a circular membrane of 400 μm in diameter and 30-μm thick. The plot was obtained using the analytical modeling described in Appendix A [1]. The deflection is higher in the
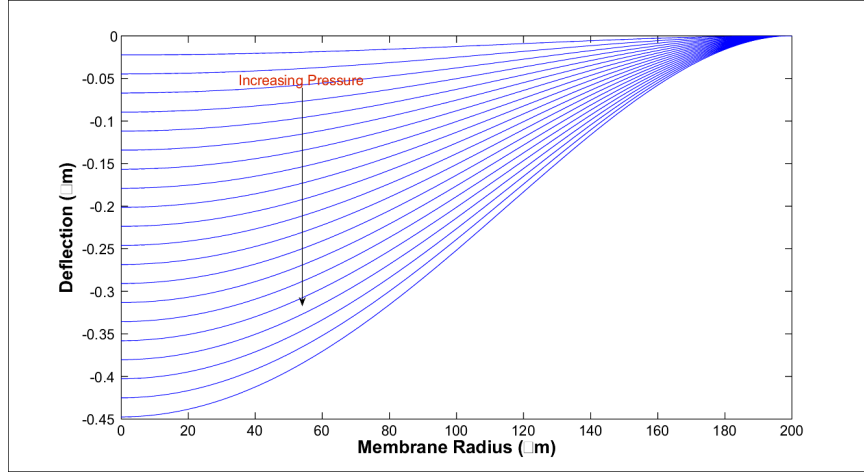
Figure 2.2: Deflection of a 400-μm circular membrane obtained using the analytical modeling detailed in Appendix A.

center of the membrane and the figure indicates that, as the pressure increases, the deflection is higher.

This type of sensor can be further classified into three distinct regimes based on the deflection of the membranes. These regimes are small deflection, medium deflection, and membrane operation. The behavior shown in Figure 2.2 falls in the small-deflection regime because its maximum deflection is kept within 30% of the diaphragm thickness, the criteria for small deflection. Diaphragms can be circular or rectangular. Circular membranes, such as the one shown in Figure 2.1 are characterized by radial and tangential stresses. Figure 2.3 shows (a) the schematic of a circular membrane depicting the direction of the radial and tangential stresses, (b) the radial and (c) the tangential stress distribution of a circular membrane, with the same dimensions as in Figure 2.2, that is rigidly clampled around its perimeter. Note that both the radial and tangential stress are equal at the center of the membrane (r=0).

2.2 Finite Element Analysis of MEMS

Finite element analysis (FEA) is a powerful tool because it allows designers to visualize and study the design, construction and subsequent device behavior. From

5
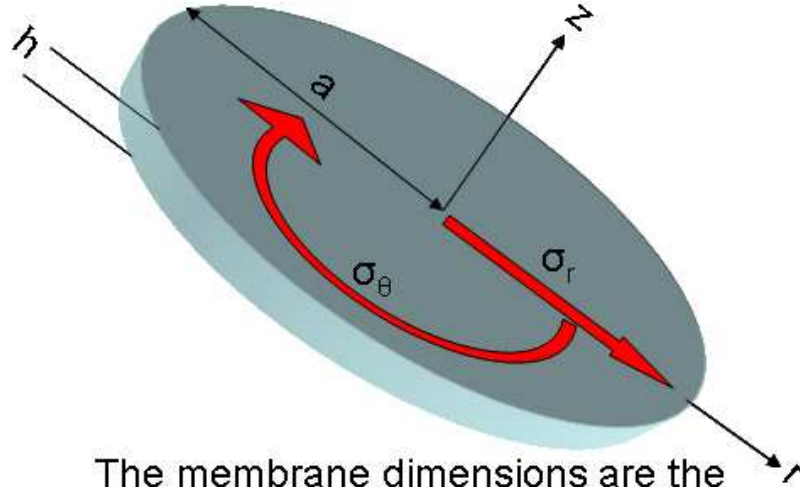
The membrane dimensions are the radius **a** and the thickness **h**

σ_θ and σ_r represent the tangential and radial stress, respectively

(a)
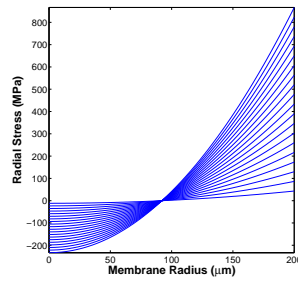
(b)
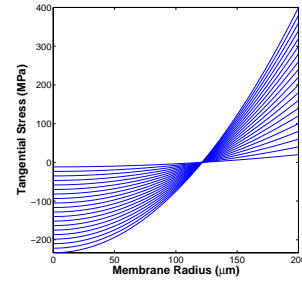
(c)

Figure 2.3: (a) Representation of a circular membrane highlighting the thickness h and radius r. It also shows both the tangential (σ) and radial (σ_r). (b) Radial stress distribution of a circular membrane with 400-μm diameter and 30-μm thickness plotted using the analytical model outlined in Appendix 1. (c) Tangential stress distribution of a circular membrane with 400-μm diameter and 30-μm thickness plotted using the analytical model outlined in Appendix 1.

.

6

a MEMS perspective, the use of FEA is a cost-saving technique that can be used to optimized the properties or behavior of MEMS designs. For instance, FEA has been widely used in mechanical engineering to predict the response of parts to an applied load. The part is represented by smaller regions so they can be meshed. Each one of these elements, in turn, is comprised of nodes and edges/corners that interact with the other elements to yield the response sought [1]. FEA is computationally demanding and a number of software suites are available to the designer to perform the analysis. ANSYS, ConventorWare, and Intellisuite are some of the many examples of software packages created to perform the analysis required.

To illustrate the value of FEA, Figure 2.4 (a) shows a polysilicon micro-mirror designed in Ledit (Ledit is the layout editor for MEMSPro, which is a personal computer based MEMS design tool) and later fabricated using the polysilicon multi-users microelectromechanical systems process (PolyMUMPS) as requirement for the MEMS curriculum at AFIT. PolyMUMPS is a surface micromachining process that consists of three structural polysilicon layers and a metal layer. The three poly-silicon layers are identified as Poly0, Poly1, and Poly2. The mirror is fabricated with the Poly2 layer. For actuation, a micro-mirror employs the capacitive property of electrodes, in which a voltage differential applied between the electrodes results in a charge fluctuation. The purpose of designing and subsequent fabrication of these micro-mirrors was to model and later test their actuation in the laboratory. Figure 2.4 (b) shows the three-dimensional model of the polysilicon micro-mirror. It shows a model of the full-size mirror, as well as a symmetrical, quarter portion. The quarter portion also shows the electrostatic and reaction forces and moments that act on the micro-mirror.

FEA results obtained for the micro-mirror are presented in Figure 2.5. Figure 2.5 (a) shows the maximum deflection obtained. The picture clearly shows how the anchor remains fixed while the rest of the flexure and micro-mirror experience deflection. The voltage was applied to the top of the micro-mirror while the substrate was grounded. Figure 2.5 (b) shows the Von Mises stress in the micro-mirror. Von Mises stress is single value of stress derived from the stress tensor so it is easier to determine

7
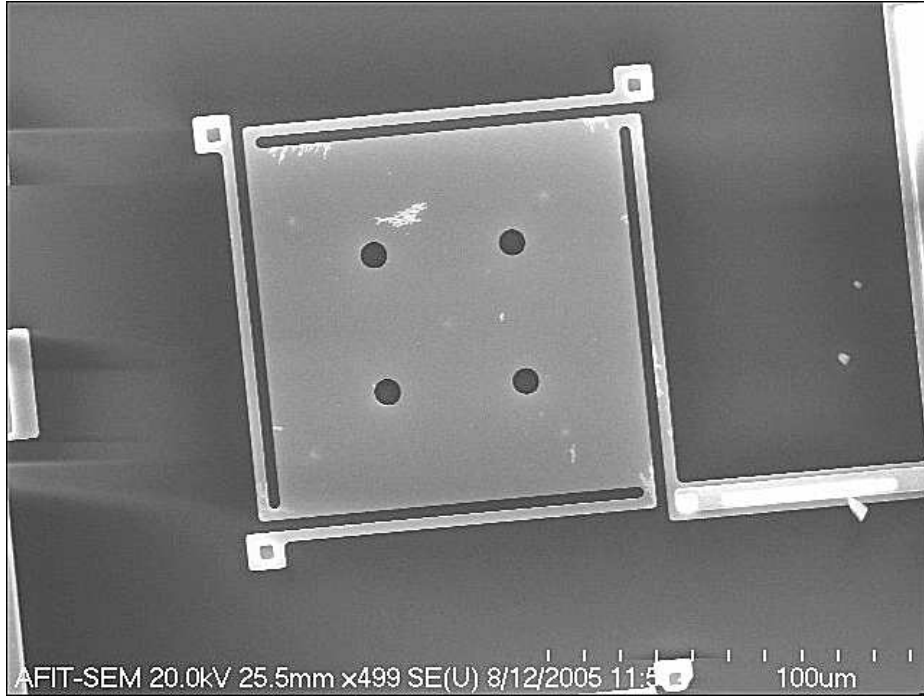
(a)
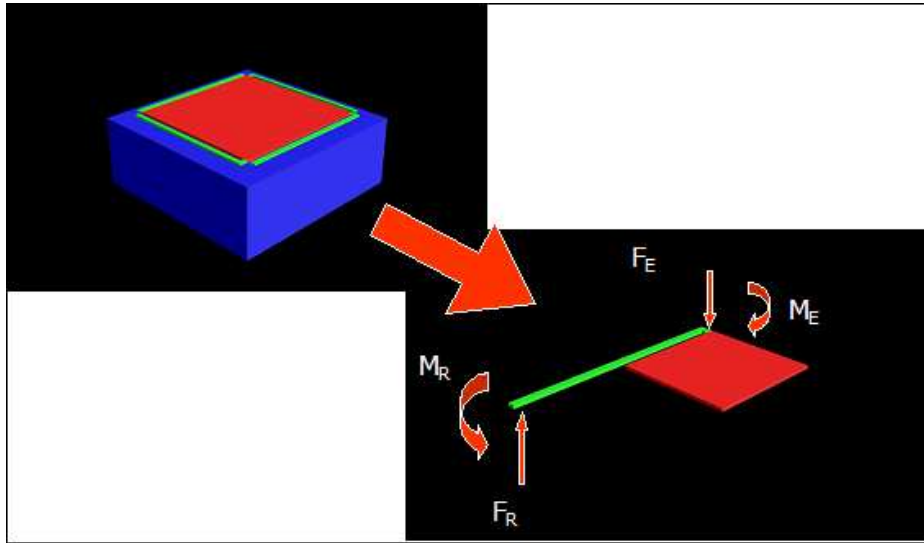
(b)

Figure 2.4: (a) SEM picture that shows the Poly2 micro-mirror at a magnification of 20.0 kV, 499X. It also shows the dimension of the micro-mirror, which is a square of 100 μm per side. The flexures on the mirror are also 100 μm. The picture also shows some of the damage the structure sustained during release and handling. (b) Three-dimensional model of the poly-silicon micro-mirror. It shows a model of the full mirror, as well as a symmetrical quarter-space portion of the full mirror. The electrostatic (M_E, F_E) and reaction (M_R, F_R) forces and moments that act on the mirror are also shown in the quarter-size portion.

.

8

the fatigue failure in a material. The stress state in the micro-mirror corresponds to the maximum deflection shown in Figure 2.5 (a). The stress is concentrated at the anchor and the link between the flexure and micro-mirror. These areas are marked in the picture.

2.3   Wide Bandgap Semiconductors

Along with fabrication, the choice of material is important. Finding a MEMS material has to be driven not just by the suitability of each fabrication process but also by factors such as cost, properties, ease of control and processing, reliability, and environment compatibility. MacDonald discusses three requirements for MEMS materials: compatibility with silicon technology, desirable electromechanical properties, and low residual stress [2]. Compatibility with silicon is critical because of integration with microelectronics. Low residual stress is also very important because devices might develop non-ideal effects (*i.e.*, excessive buckling). It is, however, crucial that stress be controlled so performance of the device can be accurately predicted [18].

Historically, micropressure sensors have been micromachined silicon devices. Technological advances in microelectronics have provided MEMS designers with well characterized materials that can be used in the type of harsh environment mentioned in the introduction. WBG semiconductors are capable of operating at temperatures far exceeding ambient temperatures. Silicon devices begin to experience problems in power consumption, internal heating, and ultimately higher current leakages at temperatures in excess of 200 degrees Celsius.

WGB materials can be defined as those with an energy bandgap exceeding 2.2 electron volts (eV). They typically include the II-oxygen, II-sulphur, II-selenium, III-nitrogen, silicon carbide (SiC) and its many polytypes, and diamond and its various alloys. Diamond, for instance, has the highest thermal conductivity of any material and very high dielectric strength.
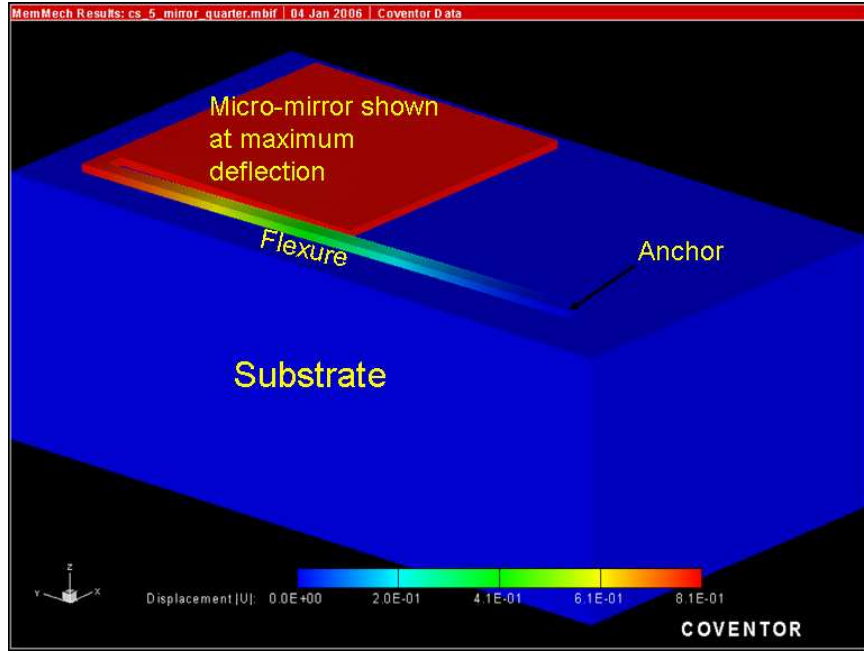
(a)
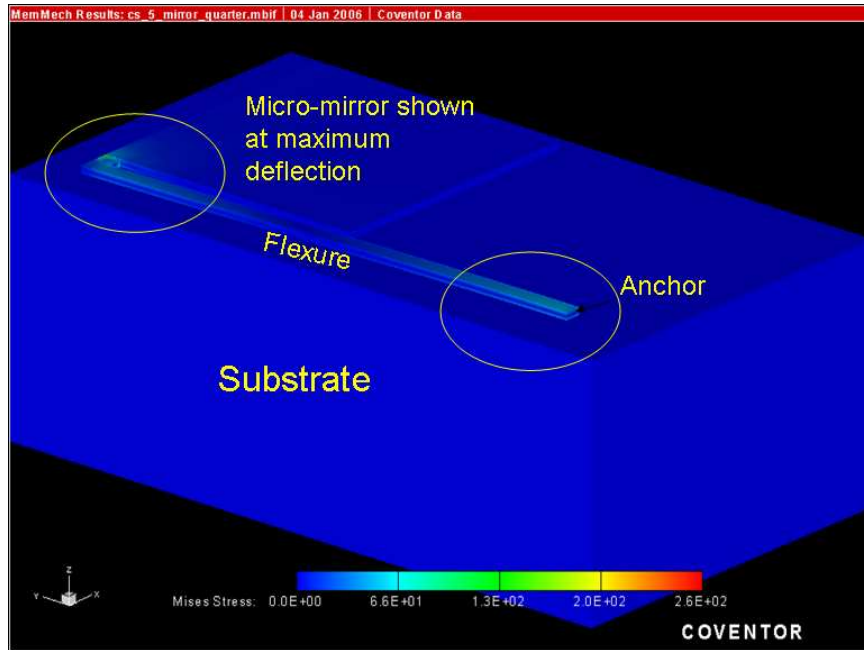
(b)

Figure 2.5:   (a) FEA results showing the maximum deflection experienced by the micro-mirror as a voltage differential between the top electrode (the mirror) and ground (the substrate) is attained. (b) FEA results showing the Von Mises stress experienced by the micro-mirror as a voltage differential between the top electrode (the mirror) and ground (the substrate) is attained. This stress state is for the condition of maximum deflection.

10

The sensor shown in Figure 2.1 is fabricated out of the 6H-SiC polytype. SiC is a well known material for microelectronics and MEMS, and extensive research has been done on its properties and fabrication. It exhibits polytypeism, meaning that it crystallizes into many different polytypes. Polytypes differ in the way the atoms stack when they form a lattice. The 6H-SiC sensor relies on the piezoresistive properties of SiC.

The III-nitrogen compounds are important compounds in electronics because of their physical properties, which include a large bandgap, considerable hardness and high thermal conductivity. These compounds have been successfully used as short-wavelength electroluminescent devices. Of the III-nitrogen compounds, gallium nitride (GaN) is particularly attractive for MEMS applications because of its high chemical inertness. AFRL/MN is particularly interested in designing micropressure sensors suitable for harsh environments, and it is this high chemical inertness that makes GaN a viable choice. However, for MEMS applications, a material must have a releasable layer so device features could be achieved. GaN does not have a natural oxide that could fit in this role. The literature research yielded limited information on successful wet etching of GaN.

GaN is typically grown on c-plane sapphire by metal-organic chemical vapor deposition (MOCVD) and molecular beam epitaxy (MBE). MBE is more advantageous than MOCVD because the growth rate is slow, growth temperature is relatively low, one can achieve atomically smooth surfaces, in-situ growth monitoring is possible, and all MBE deposition steps can be fully automated [12]. GaN crystallizes in the wurtzite structure, with space group $P6_3mc$ (no. 186). A wurtzite structure consists of alternating planes of Ga and N pairs stacked in an ABABAB sequence. This stacking means that atoms in the first and third layers are aligned. Figure 2.6 shows the wurtzite structure of GaN as viewed from the [0001] direction, as well as the ABABAB structure arrangement.

(a)

● Nitrogen
○ Gallium

[0001]

[1$\bar{1}$00]

[11$\bar{2}$0]
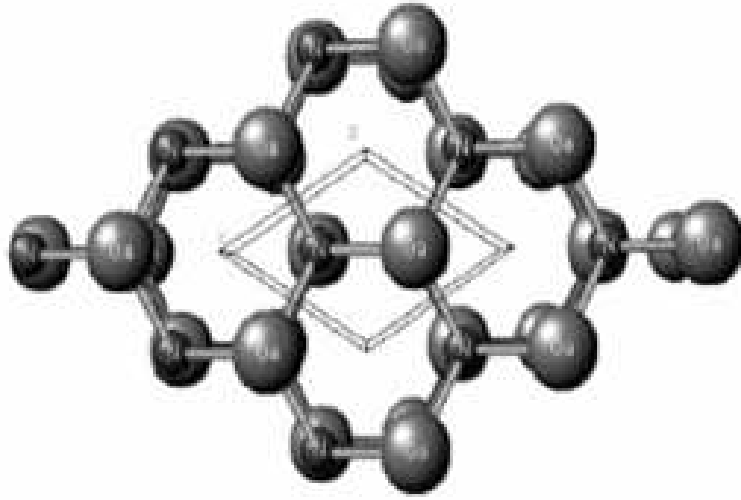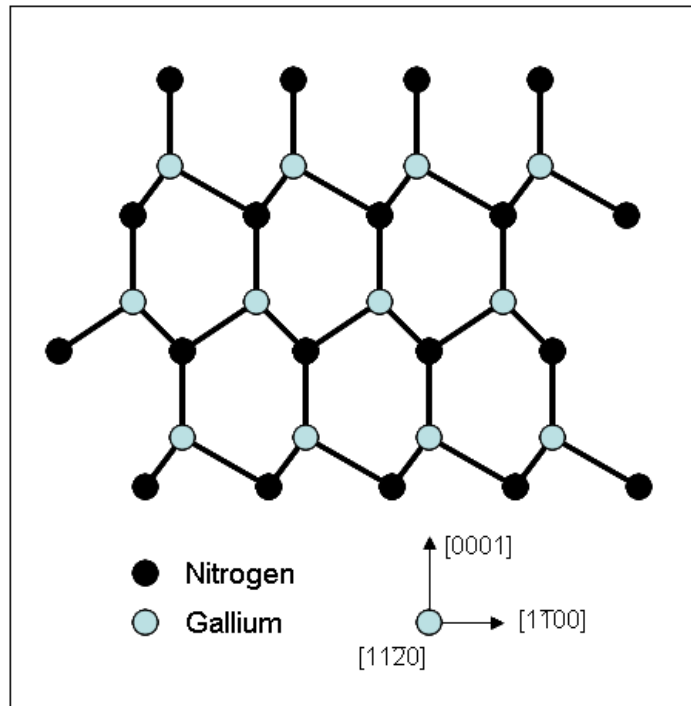
(b)

Figure 2.6:   (a) Wurtzite GaN structure as viewed along the [0001] direction. The large spheres are the Ga atoms and the smaller spheres represent N [11]. (b) ABABAB arrangement of the hexagonal wurtzite structure of GaN.

The heteroepitaxial films grown by either growth method draw their properties primarily from the substrate on which they are grown. The determining factor for a material to be used as a substrate for GaN is the lattice constant mismatch. Table 2.1 shows the percentage lattice mistmatch for some selected GaN substrates. Note that sapphire has the higher lattice mismatch percentage. The coefficient of thermal expansion is another important characteristic of the substrate that will influence the quality of the heteroepitaxial film. Sapphire has a higher coefficient of thermal expansion than GaN and the difference ultimately results in a compressive strain in the film.

Table 2.1:   GaN substrate and their percentage lattice mismatch [12].

Material	c-Lattice constant (nm)	a-Lattice constant (nm)	a-Lattice % mismatch
GaN	0.5185	0.3188	0.0
Sapphire	1.299	0.4758	-14
6H-SiC	1.511	0.308	2.3

Film doping is another source of strain. The dopant atoms become sources of hydrostatic strain that effectively change the lattice parameters. This type of stress is physically different than the biaxial stress mentioned above. Some of the defects associated with the heteroepitaxy of GaN arise from the substrate used and include high dislocation densities (primarily edge dislocations) because of the a-lattice constant mismatch, and antiphase boundaries because of the c-lattice constant mismatch. Sapphire, for instance, could result in dislocation density as high as 10^{10} cm^{-2} in the film [11].

Sapphire can be described as a hexagonal structure of six close-packed (0001) planes of oxygen ions sandwiched between 12 planes of aluminum ions. It is mainly composed of ionic bonds and has the space group $R\bar{3}c$ (no. 167). Figure 2.7 shows the (0001) view of the hexagonal unit cell of sapphire.

Sapphire presents other disadvantages to the growth of GaN. It has a very low thermal conductivity that results in poor heat dissipation. Its energy bandgap at
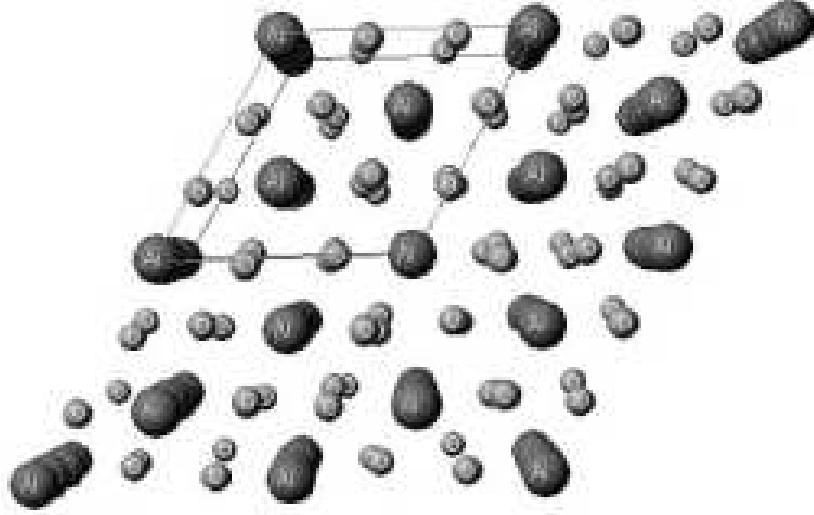
Figure 2.7:   View along the (0001) direction in the hexagonal unit cell of sapphire. The large spheres are the Al atoms and the smaller spheres are the O atoms [11].

room temperature is approximately 8.6 eV, thus making it an insulator. This further complicates device fabrication because electrical contacts cannot be made to the back side (the substrate side) of devices. Heteroepitaxial GaN films grown on c-plane sapphire usually result in c-plane films, but with a 30% rotation of the in-plane GaN crystal orientation with respect to the same direction in sapphire. This rotation helps reduce the lattice constant mismatch, which would otherwise be 30%. The use of buffer layers of aluminum nitride (AlN) or even GaN has resulted in very smooth GaN films [11].

2.4   Micro-Raman Spectroscopy

Researchers have used this non-destructive technique for determining the state of stress in a material. The Raman effect can be simply explained as scattering. When a photon of light interacts with a material, it will either be absorbed, scattered, or simply pass through without any effect. Absorption results when the incident photon has the same energy level as the gap between the ground state and an excited state; the absorption is observed by the promotion of electrons to higher energy levels. Scattering on the other hand results from the interaction between the photon and

14

the material. In Raman spectroscopy, the incident light, which is a single frequency of laser radiation, generates scattered radiation from the material at one vibrational unit of energy from that of the incident light. The ability to measure this vibrational unit of energy is the underlying detection mechanism in Raman spectroscopy. Raman spectroscopy does not have any energy requirement (such as matching the energy gap between the ground and excited state of an electron) because the light will interact with the material and distort the electron cloud (or molecules) to a point that it yields a short-lived virtual state. It is important to recognize that two types of scattering will result from the interaction between the incident photon and the material: 1) The dominant effect is an elastic-type scattering called Rayleigh scattering. Essentially, the photon-material interaction results in very small frequency changes. 2) The weak process is an inelastic-type scattering called the Raman scattering. In this case, energy is transferred from the material to the photon, or vice versa, and the energy of the scattered photon is indeed different than that of the incident photon by the one vibrational unit, as mentioned above.

In terms of energy exchange, Raman scattering can be explained as follows: the incident photon imparts some its energy, $h\nu_i$, to the lattice, which results in a phonon of energy, $h\nu_o$, and a remaining photon of lessened energy, $h\nu_s$, as described by equation (2.1). This frequency shift is known as Stokes scattering. Usually, this re-emission of a photon is isotropic and it can be observed at some angle to the exciting energy. It is important to point out that when the energy of the incident beam is higher than the bandgap of the material, the transition that occurs is much stronger.

$$h\nu_s = h\nu_i - h\nu_o \qquad (2.1)$$

If the lattice of the material is already in an excited state because of induced phonons (*i.e.*, from other incident photons or due to thermal energy), the photon that is re-emitted can be of greater energy than the incident photon, as shown by $h\nu_{a-s}$ in equation (2.2). This frequency shift is known as anti-Stokes scattering. The anti-

15

Stokes mode is generally much weaker than the Stokes mode because the phonons that participate in absorption are much lower than those that can be emitted. The phonons that can be emitted, however, will result in more anti-Stokes modes. In these cases, the intensity of both modes will be comparable. This clearly represents a case of conservation of energy.

$$h\nu_{a-s} = h\nu_i + h\nu_o \tag{2.2}$$

In addition to conservation of energy, momentum must also be conserved in these interactions. The momentum of a wave is given by $\hbar k$, where k is the propagation vector of the wave, and $\hbar$ is Plank's reduced constant. The momentum of the phonons is significantly larger than the momentum of the photons. The range of momentum available to the phonons is up to $k = 2\pi/a$, where a is the lattice constant of the material. The momentum of the photon, on the other hand, is given by $k = 2\pi/\lambda$. To satisfy momentum, two or more phonons are emitted. In semiconductor materials, these phonons are usually two transverse optical modes (TO), two transverse acoustical modes (TA), one longitudinal optical mode (LO), and one longitudinal acoustical mode (LA) [17].

Raman spectroscopy has been used for the analysis of mechanical stress since 1970 when Anastassakis *et al.* first studied the effect of uniaxial stress on optical phonons of a diamond-type lattice [5]. μRaman spectroscopy is a valuable non-destructive tool for determining localized stress states in materials. The term, μRaman, is used because of the $\leq$ 1-μm spatial resolution that can be obtained. The technique has been successfully performed at AFIT by LaVern A. Starman in his doctoral dissertation, "Characterization of Residual Stress in Microelectromechanical Systems (MEMS) devices using Raman Spectroscopy [19]," Stanley J. Ness in his thesis, "Stress Analysis of Silicon Carbide Microelectromechanical Systems using Raman Spectroscopy [14]," and John C. Zingarelli in his thesis, "Detection of Residual Stress in SiC MEMS using μRaman Spectroscopy [20]."

16

Figure 2.8 (a) shows the residual stress along the length of a 100-μm polysilicon (poly1 layer) cantilever fabricated with the PolyMUMPS process. The stress was analyzed by applying the polysilicon phonon deformations found by Starman [19]. For comparison, Figure 2.8 (b) shows the residual stress found by Starman on a similar cantilever. The difference in the slope can be attributed to the deflection of the cantilevers. The cantilever tested deflected upwards when released, contrary to Starman's cantilever. Furthermore, the stress in the cantilever is affected by the localized heating that results from the laser power incident on it.

(a)   (b)
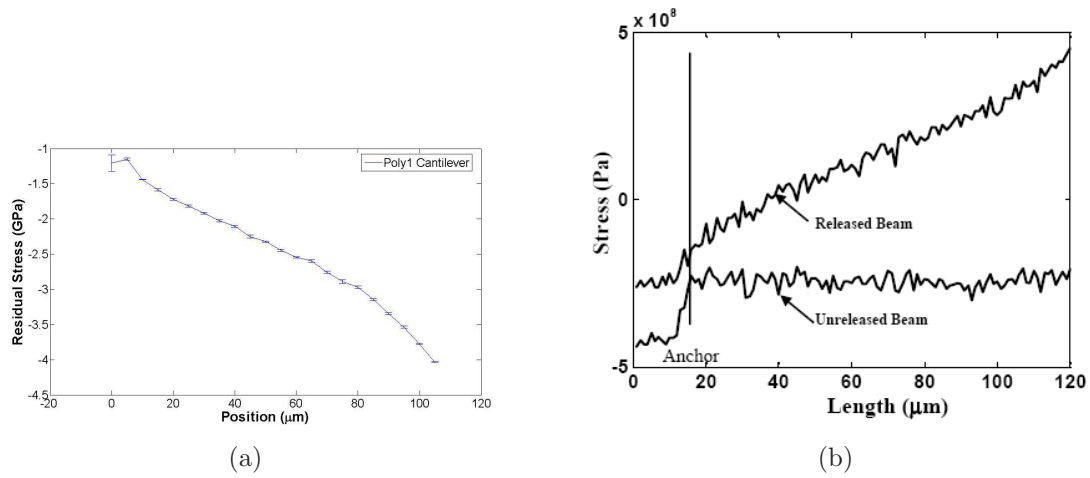
Figure 2.8:   (a) Residual stress of a 10 by 100-μm^2 polysilicon cantilever fabricated out of the poly1 layer using the PolyMUMPS process. (b) Residual stress of a 10 by 100-μm^2 cantilever designed and analyzed by Starman [19].

Zingarelli used μRaman spectroscopy to map the residual stress in 6H-SiC accelerometers. He was able to show the areas in the diaphragms where the stress is higher, as well as defect areas in the material. Figures 2.9 (a) and (b) show the NASA accelerometer fabricated out of 6H-SiC. Zingarelli tested the device by collecting raster scans along the edge of the diaphragm. Figures 2.9 (c) and (d) show the square area where the raster scan was collected, as well as the stress distribution. As can be seen in the figure, the stress is higher along the edge of the diaphragm.

μRaman spectroscopy has been useful for analyzing epitaxial GaN. It can be used to determine the stress/strain in the film similar to the work already performed

17

(a)

(b)

(c)

(d)
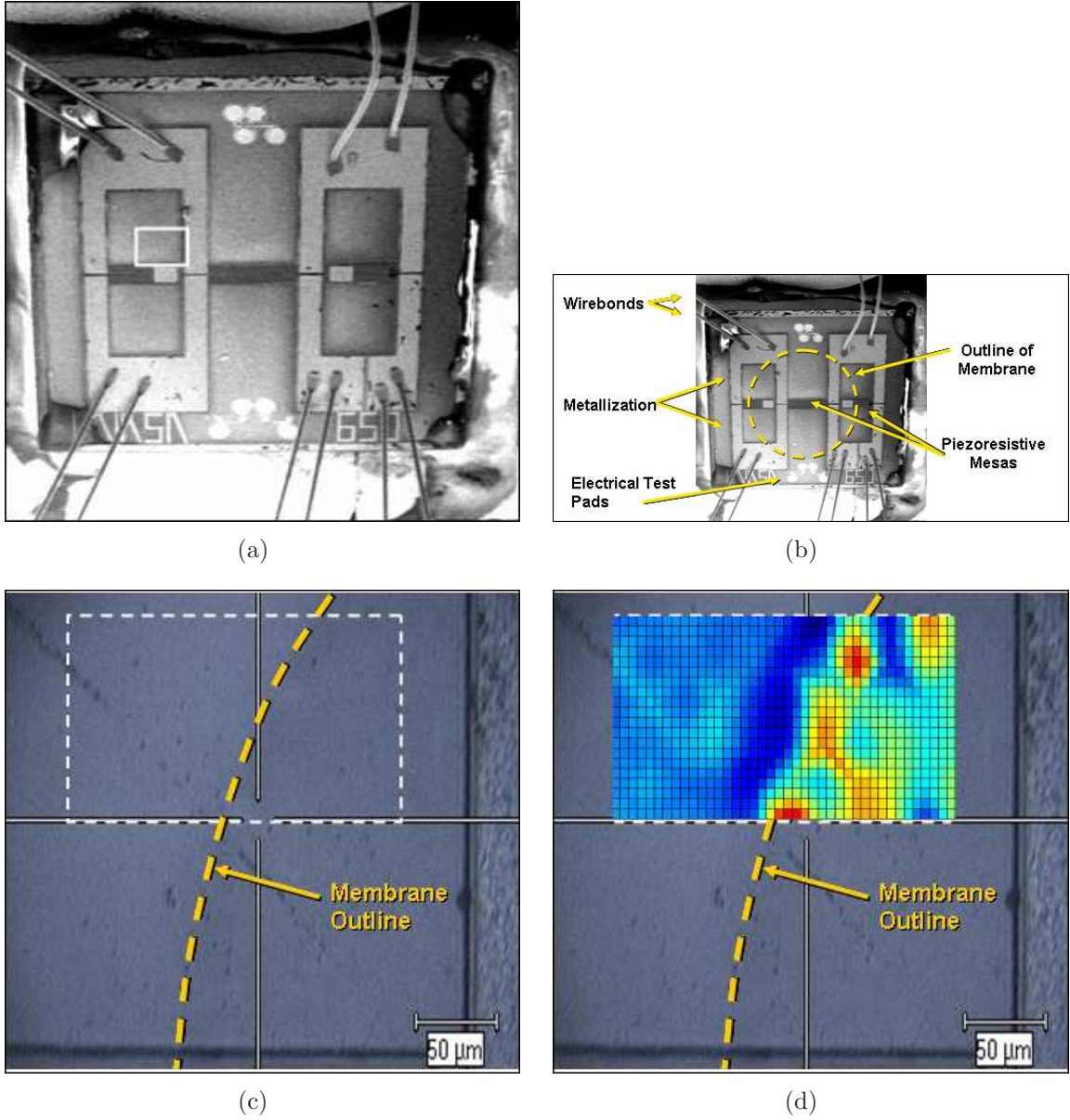
Figure 2.9: (a) SEM picture of the NASA 6H-SiC accelerometer tested by Zingarelli. (b) Annotated SEM picture of the NASA 6H-SiC accelerometer showing the diaphragm and main components. (c) Zoomed area on accelerometer (square shown in picture (a)) showing the edge the diaphragm. (d) Stress distribution, along the edge of the diaphragm, obtained using $\mu Raman$ spectroscopy [6].

18

in Si and SiC [14, 19, 20], as well as the film quality. As mentioned before, GaN in the stable state crystallizes in the wurtzite structure. Group theory predicts four Raman active modes represented by $A_1 + E_1 + 2E_2$. The A_1 and E_1 modes split into LO and TO components. The E_2 modes are nonpolar modes. In the backscatter geometry with the incident light along the [0001] direction, selection rules allow the E_2 and A_1 LO modes to be detected. For a more detailed explanation, refer to reference [16]. Figure 2.10 shows a typical Raman spectra of GaN; the top spectrum reflects the case in which the incident and scattered polarizations are perpendicular to each other and only the $E_2(H)$ is detected; when the incident and scattered polarizations are parallel, both the $E_2(H)$ and the $A_1(LO)$ are observed as shown in the bottom spectrum. The unstrained $E_2(H)$ phonon frequency is 567 cm^{-1} and the unstrained $A_1(LO)$ is 734 cm^{-1} [10].
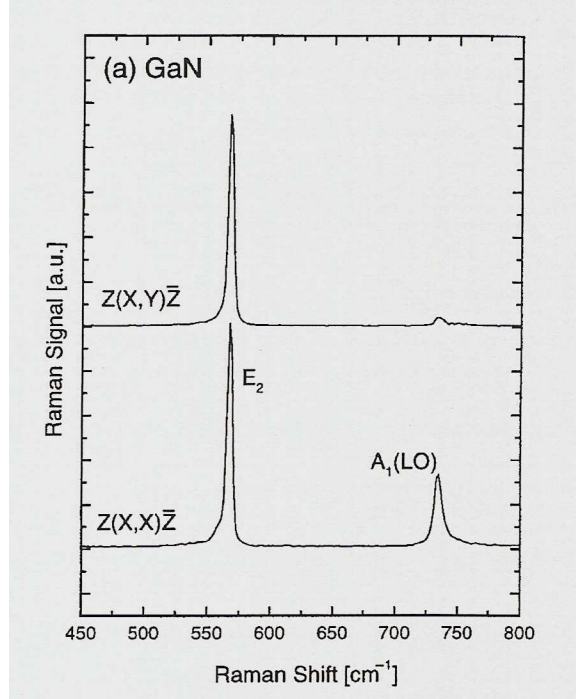
Figure 2.10:   Raman spectra of wurtzite GaN at room temperature showing two polarization configurations and the allowed phonons based on the configuration. The top spectrum reflects the case in which the incident and scattered polarizations are perpendicular to each other and only the $E_2(H)$ is detected. The bottom spectrum shows the case when the incident and scattered polarizations are parallel, in which case both the $E_2(H)$ and the $A_1(LO)$ are observed [10].

19

Sapphire, the most common substrate for heteroepitaxial GaN, has seven active phonon modes based on its group theory symmetry $(2A_{1g} + 5E_g)$. After an thorough literature search for this research it is concluded that the stress/strain and Raman peaks relationship for sapphire has not been established. The relationship between stress/strain and Raman peaks will be established in this thesis. Figure 2.11 shows an example of a sapphire spectrum for a sample that had been cooled in liquid nitrogen for two years. The peaks agree with the expected maxima located at 376, 414, 428, 440, 573, 642, and 748 cm^{-1} [9].
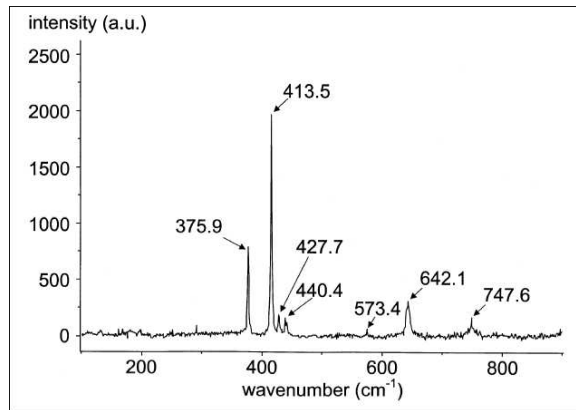
Figure 2.11:   Raman spectrum of sapphire for a sample that had been cooled down in liquid nitrogen for two years [9]

2.5   X-Ray Diffraction

The use of x-rays for evaluating materials is advantageous because the wavelength used ($\approx$ up to 0.1 angstroms) is on the order of the size of atoms so the structural properties of materials can be studied. X-rays experience two types of interactions with matter. Elastic scattering (or Thompson scattering) occurs when the incident x-rays do not lose energy when they strike the electrons of the material but rather deflect in a different direction. Inelastic scattering (Compton scattering), on the other hand, occurs when the x-rays lose energy to the electrons, which implies their wavelength will change in the process. XRD relies on Thompson scattering to obtain information about the material under investigation. The usefulness of XRD is

that all the diffracted waves can experience constructive interference and the resultant pattern will have peaks of maximum intensity that correspond to the arrangement of the atoms in the material. These peaks are governed by Bragg's law:

$$2d\sin\theta \;=\; n\lambda \qquad\qquad (2.3)$$

where λ is the wavelength of the x-ray, θ is the scattering angle, d is the distance between lattice planes, and n is the order of the diffraction peak.

Modern instruments vary in their capabilities, but a typical spectrum consists of an intensity (counts per second) versus a detector angle (θ or 2θ depending on the instrument configuration). XRD can be used to estimate the quality of a crystal by rotating the sample under investigation through θ (or ω, which is another symbol typically used to express the same angle) while the detector is maintained at a known Bragg angle, 2θ. The intensity of the spectrum obtained (counts/sec versus θ or ω) is known a "rocking curve." Another type of scan is the "omega-theta" scan ($\omega - 2\theta$), in which the source remains fixed, but if the sample rotates θ, then the detector rotates 2θ. This type of scan is useful for determining the structural composition of the material (the layers). Both types of scans are called symmetric scans and are useful for determining the quality of the material.

In heteroepitaxial GaN films, x-ray rocking curves have been used to measure the peak position of GaN, strain in the film and substrate, and peak widths. These measurements can lead to the determination of stress in the film and substrate, as well as defects in the material (dislocation types and densities) [11].

2.6 Summary

This chapter provides a brief introduction to MEMS micro-pressure sensors and material considerations, specifically GaN on c-plane sapphire. It also introduces FEA modeling for MEMS and provides a brief description of μRaman spectroscopy and

XRD. The information provided serves as necessary background for the understanding of upcoming chapters.

III. Samples and Circular Membrane Design

MEMS are usually created in three distinct processes. First, the features of the device are layed out in a computer software. Second, the designs are submitted to a foundry for fabrication. Last, the devices undergo a series of post-fabrication steps such as release, bonding, packaging, and integration. The designer will design the device according to established design rules of the fabrication process. PolyMUMPS, for instance, publishes design rules for MEMS fabricated using this process and the foundry guarantees the features, provided the rules are followed. Just as important to the designer is knowing the suitability of the material for the devices. The first section in this chapter describes the wafers used for the fabrication of the circular membranes. The fabrication process of these membranes is then covered in the second section.

3.1 Wafers

The GaN heteroepitaxial films were grown by gas source MBE on 3-inch c-plane sapphire ($Al_2O_3(0001)$) wafers. MBE is a process in which thin films are deposited on clean surfaces of single-crystalline substrate held at high temperatures under ultrahigh vacuum conditions. The deposition is done by reacting thermal beams of atoms or molecules on the substrate. It is a physical process of depositing films [12]. The wafers were grown by Dr. Joe Van Nostrand from the AFRL's Materials and Manufacturing Directorate (AFRL/ML), Wright-Patterson Air Force Base, with a Varian 360 MBE system using ammonia as the nitrogen source. A buffer layer of AlN is deposited onto the substrate after a 1-min exposure of the substrate to ammonia for stabilization of the ammonia flux. The purpose of this buffer layer is to improve the quality of the GaN main layer (helps alleviate the lattice mismatch in the GaN film). Elemental aluminum and gallium are supplied at a rate of 0.5 $\mu m - h^{-1}$ from standard Knudsen cells. Table 3.1 shows the layers grown in each wafer, respective thickness, and dopant (if known).

There were problems in the growth of wafers A812 and A813. Outgassing of the ring carrier prevented film growth on the outer edge of the wafer. Furthermore, the

Table 3.1: Wafer information showing the thickness of each layer and the dopant used (if known) for each of the wafers investigated in this research [15].

Wafer	Layer	Thickness	Dopant
A342	AlN	800 $A°$	None
A342	GaN	2 μm	Silicon $(2.4X10^{17}cm^{-3})$
A812	AlN	250 $A°$	None
A812	GaN	2000 $A°$	Carbon
A812	GaN	4.8 μm	Silicon
A813	AlN	375 $A°$	None
A813	GaN	1333 $A°$	Carbon
A813	GaN	4.0 μm	Silicon

measured film thickness was less than the values shown in Table 3.1. According to Van Nostrand, the growth rate appears to drop in long growths although the cause of this drop has not been determined. He suspects the Knudsen effusion cells or changes in surface kinetics [15]. Figure 3.1 shows the mapping of the film growth for wafers (a) A812 and (b) A813. Note the significant difference in film thickness in each of the wafers, as well as the deviation from the expected thickness of 4.8 μm for A812 and 4.0 μm for A813.

3.2 Fabrication of Circular Membranes

The circular membranes for the pressure sensors investigated in this research were fabricated by Laser Mound and Photonic Center, Inc., Miamisburg, OH using a technique known as micromachining laser drilling. The drilling was done using a pulsed Spectra-Physics, Third Harmonic Vanadate ($Nd : YVO_4$) 355- nanometer (nm) laser. Unlike more traditional MEMS fabrication techniques, a mask is not defined for laser drilling. The laser beam is directed onto the sample with a scan head that is preloaded with the pattern desired. The peak power on the sample can be high and varies depending on the settings used. Traditional microprocessing techniques are not feasible with some WBG materials because of their hardness. Ding *et. al.* reported using a laser-induced backside wet etching on sapphire, in which the
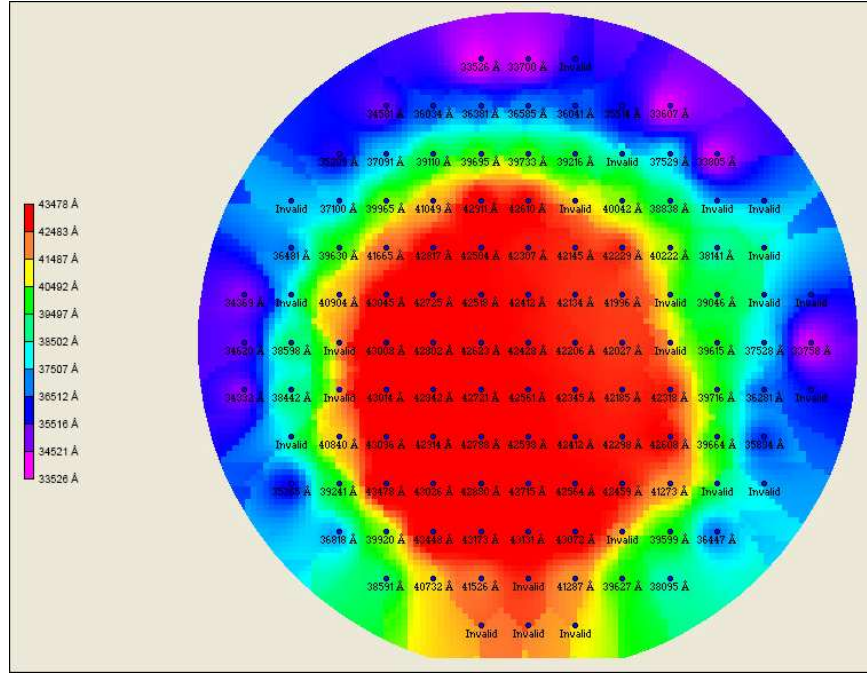
(a)
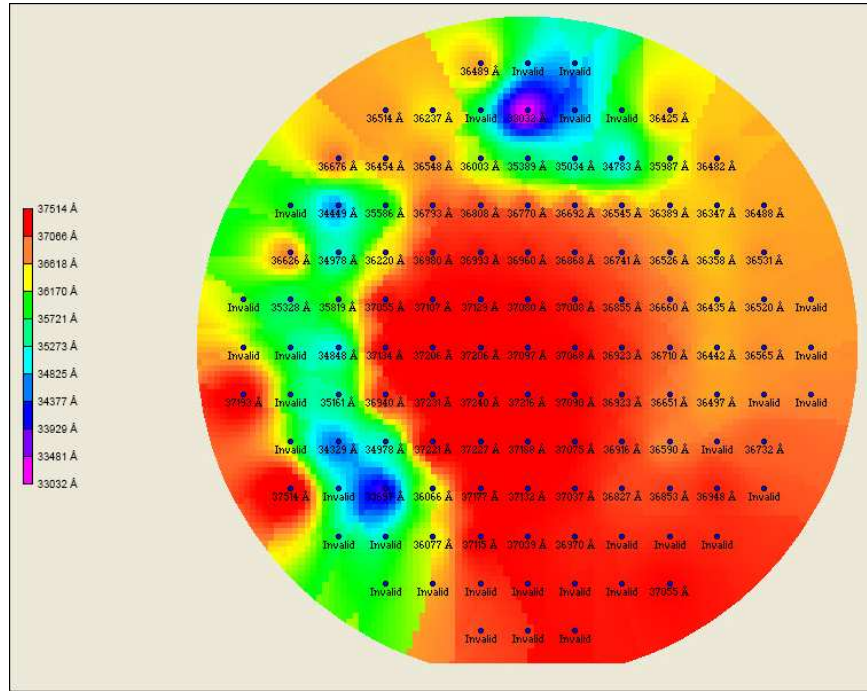
(b)

Figure 3.1:   (a) Map of the GaN film thickness in wafer A812. The thickness is not uniform throughout the wafer and deviates from the expected value of 4.8 μm. (b) Map of the GaN film thickness in wafer A813. The thickness is not uniform throughout the wafer and deviates from the expected value of 4.8 μm [15].

25

pyrene/acetone, neat toluene, or an aqueous solution of pyrene or naphtalene were used as etching media. The light source was a 248-nm KrF laser with a repetition rate of 2 hertz. They found that even though etching of sapphire was possible, the quality of the etch is not very good. Furthermore, the breakdown of the etching medium generated a thin layer of amorphous carbon film which contributed to the etching but also to the poor quality of the etch [4]. Plasma etching is another etching method for the fabrication of MEMS, but it could possibly introduce damage to the devices, thus rendering it less suitable for precise micromachining. Laser drilling, on the other hand, does not require the use of a etching medium. It is a process that selectively removes material. The foundry performed the laser drilling from the backside of the substrate. The target device features specified for the circular membranes are shown in Figure 3.2.
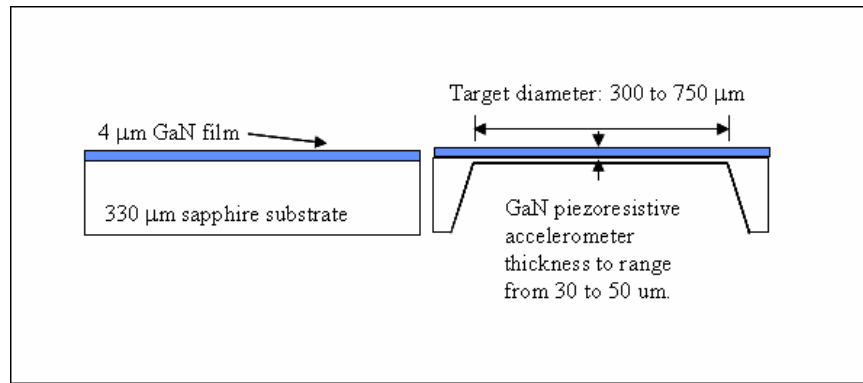
Figure 3.2: Device features and dimensions specified by AFRL/MNMF for the circular membranes [7]

3.3 Summary

In this chapter, the growth of the wafers using gas-source MBE was explained. The chapter also provides specific layer information for the grown material. The fabrication of the membranes using laser micromachining drilling was also presented. The experimental setup will be covered in detail in the next chapter.

IV. Experimental Procedure and Equipment

This chapter describes the experimental setup, as well as the equipment used during the experiments. The sections in the chapter are FEA of circular membranes, Zygo interferometry, XRD analysis and Raman spectroscopy.

4.1 Finite Element Analysis

FEA was done using the 2004 version of ConventorWare, which is a design and simulation environment for MEMS. It consists of four independent processes or bundles: designer, analyzer, integrator, and architect. The designer is the environment for designing, specifying, and modeling MEMS. The user is able to create a layout of the structure, and then generate a three-dimensional solid model from two-dimensional masks. The analyzer consists of various types of solvers or analysis tools, such as MemCap, MemMech, CoSolveEM, *etc*. All these simulations use finite element techniques and boundary conditions to appropriately solve the differential equations for each of the physical domains of the structures. MemMech, which is the tool used in this research, is the mechanical tool that analyzes structural, displacement, modal, harmonic, stress, and thermomechanical properties of devices [1].

Chapter II provided background information on the importance of modeling because it eventually leads to optimized devices. Modeling the circular membranes involves a three-step process: first, the growth sequence of the membrane is created and the features of the device are drawn using the layout tool included in the software; second, the 3D model of the membrane is created; and third, the required simulation is performed, which in the case of the circular membranes, is a mechanical simulation.

The circular membranes are fabricated on a sapphire substrate using a laser micromachining laser technique. Essentially, this process falls under bulk micromachining because material is etched away from the substrate to create the device. Laser micromachining cannot be simulated in CoventorWare. However, starting with the substrate, layers of the desired material can be added with the appropriate thickness

in order to fabricate the device. The sapphire properties used for the simulation are shown in Table 4.1

Table 4.1: Sapphire properties used in the FEA analysis of circular membranes using the 2004 version of CoventorWare.

Property	Value
Young Modulus	452000 MPa
Poisson's	0.3
Density	$3.98X10^{-15}\ kg/\mu m^3$
Thermal Coefficient of Expansion	$6.8X10^{-6}\ K^{-1}$
Thermal Conductivity	$2.508X10^7\ pW/\mu mK$
Electrical Conductivity	$1X10^5\ pS/\mu m$
Dielectric	8.0

Two models are available for the circular membrane. The first model is the full membrane and the second is just a symmetric quarter portion of it. This second model was created to take advantage of symmetry and to speed up the simulation time. Recall from Chapter II that a 3D model is broken down into smaller parts that are meshed together. The various types of mesh elements available include tetrahedral, bricks, and hexahedral. The choice is up to the user, but should be geometry-specific. The mesh was optimized for evaluation time by trying different node sizes. The mesh type for the membrane is extruded bricks mesh, pave algorithm, with parabolic volume elements of 6250 cubic units. Figures 4.1 (a) and (b) show the 3D model and corresponding mesh model for the full membrane. Not shown in the figure is the substrate. The two thin strips of GaN film on top of the membrane were arbitrarily placed symmetrically about the center line. Figures 4.1 (c) and (d) show the 3D model and corresponding mesh model for the quarter portion of the membrane. The figure shows the side walls (vias) of the membrane, which are representative of the substrate. The thin strip of GaN film was arbitrarily placed symmetrically on the membrane and the substrate (represented by the wall).

The circular membrane was analyzed using a mechanical simulation (Mem-Mech). In this type of simulation, CoventorWare yields displacement and mechanical

28
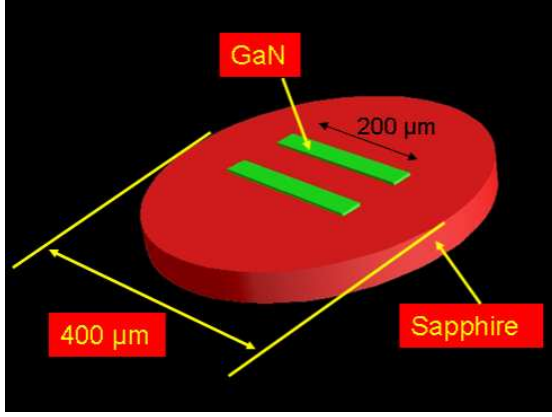
(a)
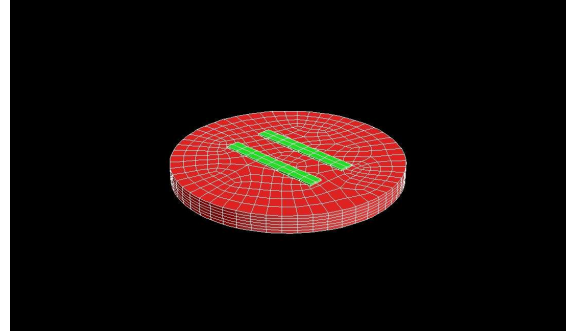
(b)
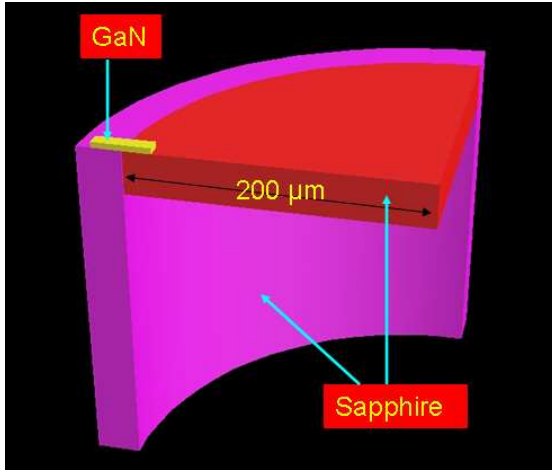
(c)
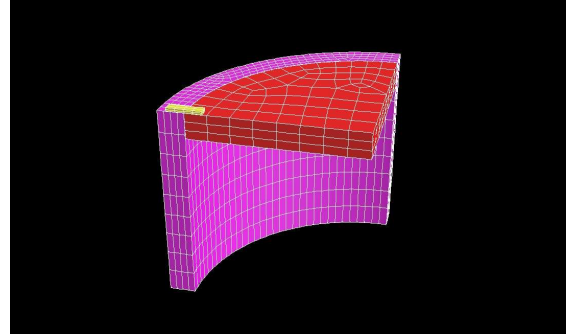
(d)

Figure 4.1:   (a) Annotated 3D model for the full circular membrane indicating dimensions and features of the device. (b) Mesh model for the full circular membrane. (c) Annotated 3D model for the symmetric, quarter-portion of the membrane indicating dimensions and features. (d) Mesh model for the quarter-portion of the membrane.

stress at each node and consequently for the entire model. Two different simulations were set up: 1) A single uniform load of 20 MPa was applied on top of the quarter-portion of the membrane; the boundary conditions included fixing the edges of the model along the x- and y-directions, and using a tied-link to the walls; the walls were not allowed to move during the simulation. 2) A load ranging from 1 to 50 MPa was applied in steps of 5 MPa to the top of the quarter portion of the membrane; the boundary conditions remained the same.

4.2 Surface Profiling

The purpose of this experiment was to physically characterize the quality of the membranes. Examining the topography of fabricated devices is a standard post-fabrication technique in MEMS technology. It is particularly important when determining the amount of residual stress because one can accurately measure deflections and/or curvature of devices. The two techniques employed to performed this characterization are by the use of an interferometry microscope and a surface profiler.

4.2.1 Zygo Interferometry. The Zygo interferometer uses white light to generate interference patterns onto a surface. The pattern, which is simply a band of dark and bright lines or fringes, occurs because of the optical path difference between the reference and the sample under investigation. Any standard optics textbook explains interferometry as splitting light inside the interfometer, with one beam directed toward an internal reference mirror and the other beam toward the sample. The reflected beams recombine and undergo constructive and destructive interference. The dark and bright lines are, in fact, the constructive and destructive interference pattern [8]. Figure 4.2 (a) shows the interferometer spectrum obtained from a series of PolyMUMPS Poly1 cantilevers. The spectrum was collected with the instrument's standard 10X objective at a zoom level of 2.0. Figure 4.2 (b) is an oblique construct of the spectrum to illustrate the elevation and deflection of the devices. The plots were obtained with MetroPro, the instrument's software.
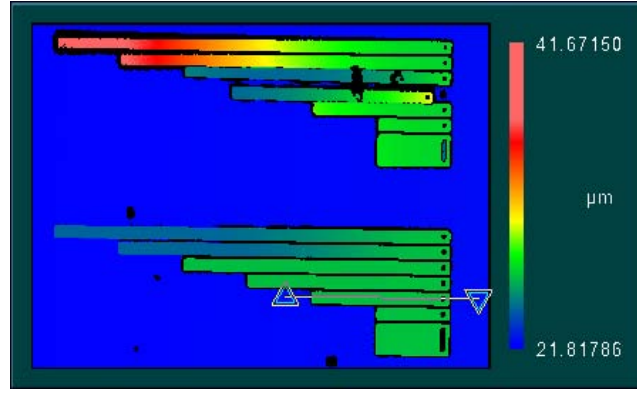
(a)
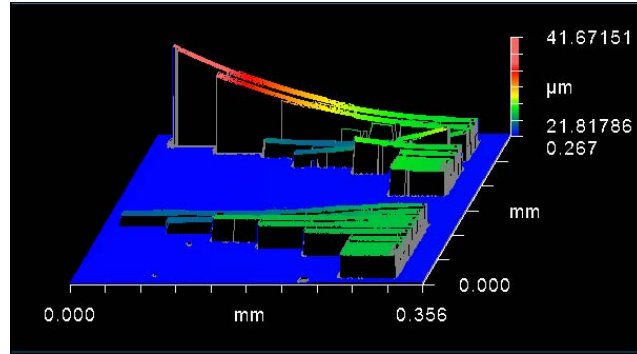
(b)

Figure 4.2:   (a) Interferometer spectrum of a series of PolyMUMPS Poly1 can-
tilevers collected with a 10X objective at a zoom level of 2.0. (b) Oblique pattern
constructed with the Zygo Interferometer's accompanying MetroPro software to show
the deflection and features of the cantilevers.

4.2.2 Surface Profiler.   Another technique for determining the quality of a
material surface is with the use of a profilometer. Profilometers are useful because they
can detect the roughness in the surface as well as other topographical features (dips,
heights, *etc.*). Figure 4.3 is a picture of the Tencor P-10 profiler used to characterize
the circular membranes. The profiler is owned by AFRL/ML.

4.3   Phonon Deformation Potential of GaN on Sapphire

μRaman spectroscopy was used to characterize the stress distribution in the
GaN epilayer grown on c-plane sapphire wafers, and fabricated circular membranes.
It is, as pointed out in Chapter II, an efficient, nondestructive technique for deter-

Figure 4.3:   Picture of the Tencor P-10 profiler

mining this distribution because of the ability to measure the spectral shift in Raman peaks in a material and correlate the shift with stress and strain. The Raman peak shift as a function of stress correlation, known as the phonon deformation potential (PDP), of both the GaN and sapphire is first determined by applying pressure to the material using a four-point strain fixture while simultaneously monitoring the applied pressure using a strain gauge, and recording the Raman spectrum. Starman successfully showed this relationship with silicon and polysilicon devices. A detailed treatment of the theory and experimental procedure is outlined in his PhD dissertation [19]. The spectral positions of the E_2 Raman mode in GaN and A_{1g} mode in sapphire are tracked in the samples, and stress distribution then determined using the PDP. The following sections describe the equipment used for this experiment.

4.3.1 μRaman Spectroscopy.   The μRaman spectra was performed using a Renishaw InVia Raman spectrometer located at AFRL/ML. The spectrometer is equipped with four excitation laser sources: a helium-cadmium ($\lambda = 325\ nm, 50\ mW$), argon ion ($\lambda = 514.5\ nm, 150\ mW$), helium-neon ($\lambda = 633\ nm, 30\ mW$), and a diode array ($\lambda = 830\ nm, 300\ mW$). Appendix B lists the instrument's technical specifications obtained from AFRL/ML. Figure 4.4 (a) shows the AFRL/ML InVia spectrometer used during this experiment. Figure 4.4 (b) is the internal schematic of the system with the main components shown in the legend.

(a)

A – Microscope objectives & Motorized XYZ stage
B – Spectrograph entrance slit assembly
C – Diffraction grating assembly   E – Beam expander
D – Holographic notch filter   F – CCD detector
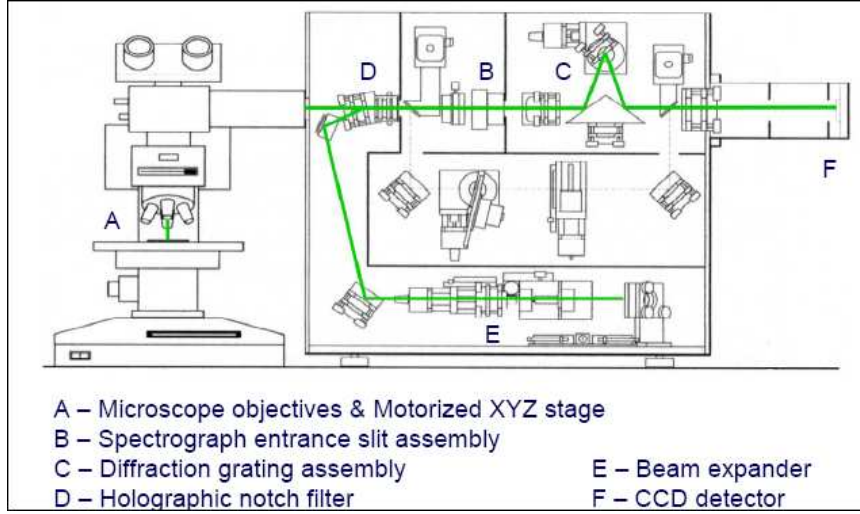
(b)

Figure 4.4: (a) Renishaw InVia spectrometer located at AFRL/ML. (b) Schematic of the internal components of the InVia spectrometer [20].

The spectral resolution of the InVia is summarized in Table 4.2. The values were obtained using $\Delta\nu = \Delta\lambda/\lambda^2$, where $\Delta\lambda = (aw)/(fm)$ where, in turn, a is the grating spacing (1200, 1800, or 2400 lines/mm), w is the slit width (50 μm), f is the focal length of the monochromator (200 mm), and m is the diffraction order (1) [20]. The approximate sampling rate is specified in Appendix B. For instance, using the 514-nm laser, the scan wavenumber resolution is approximately 2-3 cm^{-1} when using the 1800 l/mm grating.

33

Table 4.2:   Spectral resolution of Renishaw InVia spectrometer for each of the excitation sources and corresponding grating [20].

Source Wavelength (nm)	Grating (l/mm)	Resolution (cm^{-1})
325	2400	9.865
514	1200	7.884
514	1800	5.257
633	1200	5.199
633	1800	3.467
830	1200	3.024

To determine the best excitation source to collect the Raman spectra, scans were collected using the 325-, 514-, and 633-nm lasers. Because the energy bandgap of GaN is approximately 3.5 eV, the 325-nm laser ($\approx$3.8 eV) would only yield information on the surface of the GaN. The absorption coefficient of GaN at 3.8 eV is approximately 1.0X10^5, which means the 325-nm laser will examine a surface layer of approximately 50 nm using the relationship, *penetration depth* $= 1/(2\alpha)$ [13]. On the other hand, both GaN and sapphire are semi-transparent to visible wavelengths, so both the 514- and 633-nm lasers would be adequate sources for information on the GaN layer and substrate.

4.3.2 Four-point Bending Fixture.   To fully understand and derive a relationship between stress and Raman shift, it is necessary to collect a series of Raman spectra over a range of known stress values. The induced stress can be achieved with a four-point bending fixture, shown in Figure 4.5. Samples of GaN on sapphire were cut from the center of wafer A812, where the film thickness is more uniform. The samples were rectangular beams (2-mm wide by 10-mm long) that were then fixed to plexiglass rectangular beams using M-bond 200 epoxy. The strain induced in the beams is monitored with a Vishay 06-125AD-120 precision strain gauge epoxied next to the GaN on sapphire rectangular samples. The strain is read and recorded using a P-3 strain indicator. A μRaman spectrum is collected after each strain adjustment

on the samples. Because the beams experience compressive strain, it is necessary to re-focus the collecting objective onto the sample every time a strain adjustment is made.
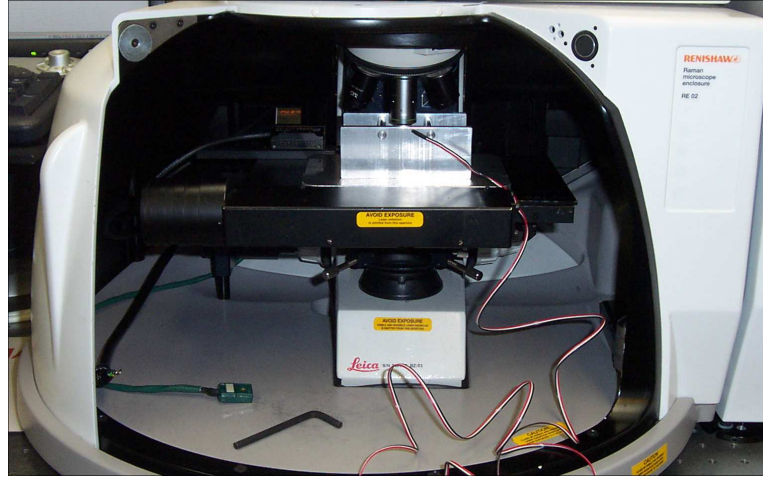
(a)
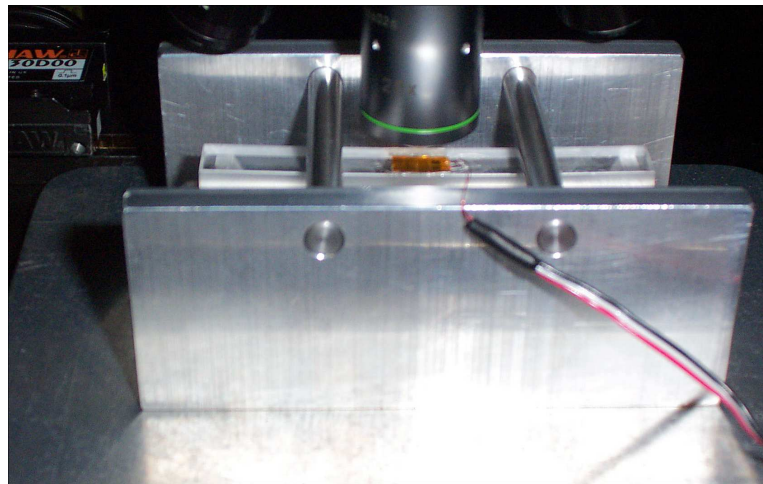
(b)

Figure 4.5:   (a) Four-point bending fixture under the Raman microscope. (b) Close-up picture of the same set up shown in (a) that shows how the sample is loaded.

4.3.3   P-3 Strain Indicator.   The P-3 Strain Indicator, shown in Figure 4.6, was used to read the induced strain in the samples of GaN on sapphire. The instrument is able to read strain gauges configured as half-bridge or full-bridge resistive elements.

Figure 4.6:   P-3 Strain Indicator

4.4   Wafer and Membrane Stress Distribution Characterization

To characterize the stress, two separate procedures were performed. The first experiment is a qualitative look at the material using XRD. As pointed out in Chapter II, XRD spectra collected on heteroepitaxial GaN films can lead to the asssesment of stress in the film and substrate, as well as defects in the material. The second experiment involves collecting Raman spectra of the material and using the PDP to quantify the amount of stress.

4.4.1 X-ray Diffraction.   Omega-theta scans obtained by XRD on the (002) plane were collected across wafer A813 in steps of 10 mm to determine the quality of the as-grown material. The other type of scan was a reciprocal space map to examine the crystalline quality of the material. The scans were done using an Xpert Pro system equipped with a germanium channel cut (220), four-bounce monochromator selecting only the copper $K\alpha_1$ wavelength ($\lambda = 0.154059\ nm$) line. Figure 4.7 is a picture of the instrument used.

4.4.2 μRaman Spectroscopy.   Single, line, and area scans were collected from the three samples described in Chapter III. Unless specified otherwise, the scans were collected at room temperature, with the 50X objective, and using the 514-nm laser at 100% laser power. The samples were analyzed in a backscatter configuration with the z-direction parallel to the c-axis of the material.

Figure 4.7:   Xpert Pro system used for all the x-ray diffraction measurements

Single scans were collected away from any fabricated membrane to ensure the scans would be representative of the film growth and quality. It also provides background results from areas not affected by the energy of the laser used during micro-machining drilling. Single scans were also taken in the membranes to quantify the quality of the material post-fabrication

Line scans were collected from representative membranes. The purpose of these scans is to quantify the stress level of the material. Figure 4.8 depicts the scan setup.

Raster scans were collected along the edge of the membranes to show the distribution of stress state that occurs from the clampled nature of the membrane. These area scans were rectangular and collected at different step sizes. These scans were done using the 20X objective. Figure 4.9 shows the setup of one of the raster scans collected, in which the step size is 5 μm for a total area of 625 μm^2.

4.5   Summary

The experimental setups were explained in this chapter. When applicable, the equipment used for the experiments was described. The results are presented in Chapter V.
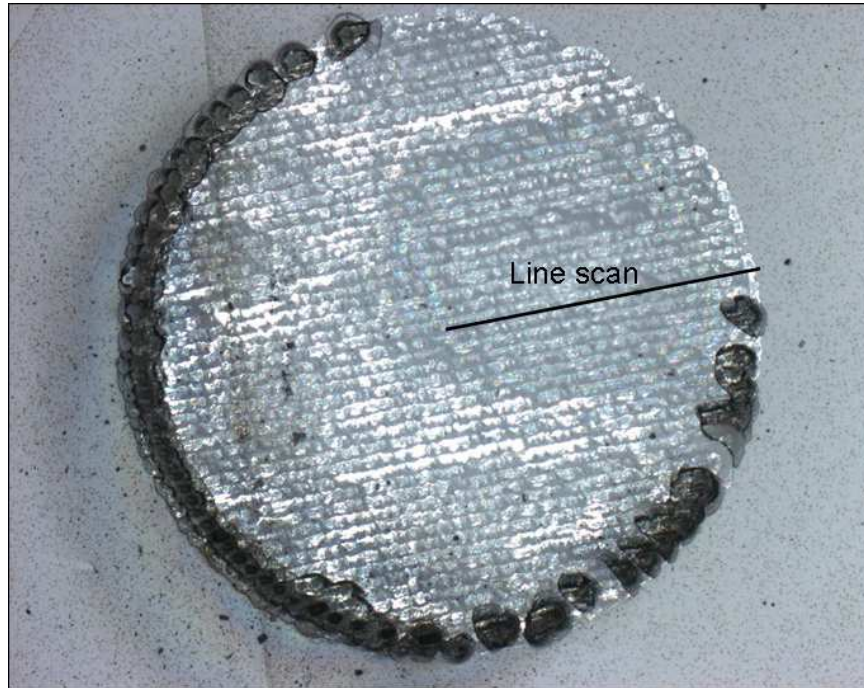
Figure 4.8:   Line scan setup. The scan goes from approximately the middle of the membrane to the edge in steps of 10 μm.
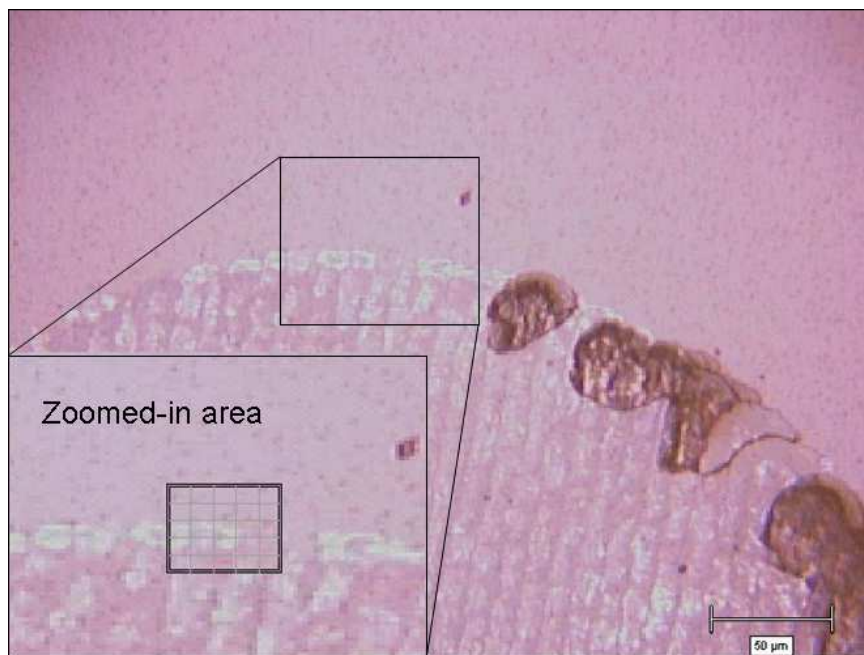
Figure 4.9:   Raster scan setup. The zoomed-in box shows the area in the membrane where the scan was collected. The raster scan area is 625 μm^2.

V. Results and Analysis

This chapter presents the modeling and experimental results obtained. Section 5.1 presents the results obtained from the FEA modeling done. The surface profiling of the fabricated membranes is shown and discussed in section 5.2. Section 5.3 presents and discusses the determination of Raman shift as a function of applied stress (phonon deformation potential). Finally, stress analysis of the fabricated membranes via single, line, and raster scans is presented in Section 5.4.

5.1   *Finite Element Analysis*

The FEA results give an insight to the behavior of the membranes. As predicted by the analytical modeling described in Appendix A, the pressure load applied uniformly on the top surface of the diaphgram results in a downward deflection, with its maximum value at the center of the diaphragm. The circular structure is clamped to the rest of the substrate. This is evident from the results because at the tied-link between the diaphgram and substrate (represented in the model by the wall), there is no evidence of deflection. The analytical results presented in Chapter II further validate this observation (Figure 2.2). Figure 5.1 shows the results obtained. Figure 5.1 (a) is the symmetric quarter portion of diaphragm modeled, and it shows the deflection that occurs from the clampled boundary to the center of the diaphragm. From the figure, the maximum deflection obtained for a pressure load of 50 MPa is approximately 13 μm. Even though the mechanical simulation increased the pressure applied from 1 MPa to 50 MPa in steps of 5 MPa, the figure only shows the result obtained when 50 MPa is impinged on the top surface of the diaphgram. Also shown in the figure is the deflection experienced by the piezoresistive GaN beam placed at the boundary between the substrate and the diaphgram. Figure 5.1 (b) shows the parametric results of deflection as a function of applied pressure. It is a linear relationship because the pressure was applied uniformly on the top surface. The results accurately show that, for 50 MPa, the deflection obtained is just under 13 μm.
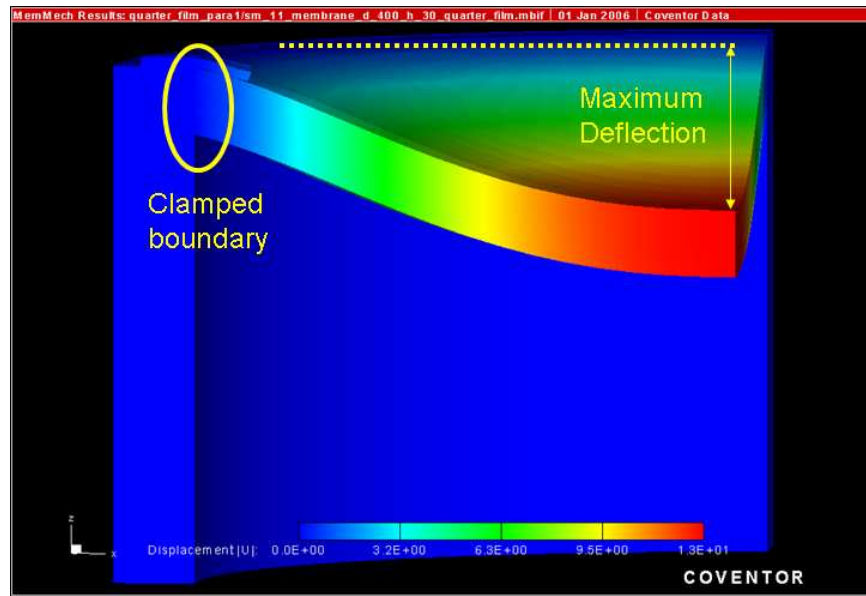
(a)
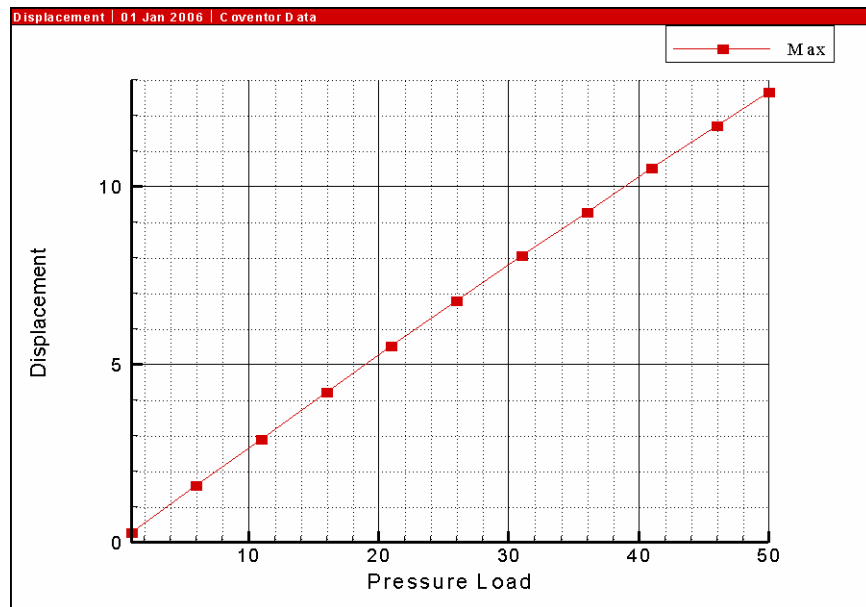
(b)

Figure 5.1:   (a) FEA model result of the deflection of a clampled circular diaphgram. The maximum deflection occurs at the center of the diaphgram. The figure also shows the clampled boundary between the diaphgram and the substrate (represented in the model by the wall). The uniformly applied pressure was 50 MPa. (b) Parametric results of the deflection at the center of the diaphram for a uniformly applied pressure ranging from 1 to 50 MPa in steps of 5 MPa.

The other characterizing factors in circular diaphgrams are the radial and tangential stresses. The analytical behavior of the circular membrane indicates the maximum radial stress occurs at the boundary with the substrate. Both the radial and tangential stresses are equal at the center. FEA results are typically presented as Von Mises stress. In this research, the Von Mises stress is used to show the generalized stress distribution in the circular membranes. Figure 5.2 shows that stress is concentrated along the boundary between the diaphragm and substrate. The radial stress distribution predicted this behavior. In the model, however, high Von Mises stress is found along the edges of the quarter portion of the diaphgram. This is simply a result of having fixed the edges of the model in the x- and y-direction. These are necessary boundary conditions to take advantage of the diaphgram's symmetry. Also shown in the plot is the effect the deflection has on the GaN film. The film strip extends beyond the diaphragm, and it is representative of one of the resistive elements in a Wheatstone bridge configuration. As expected, the stress is higher right along the boundary.
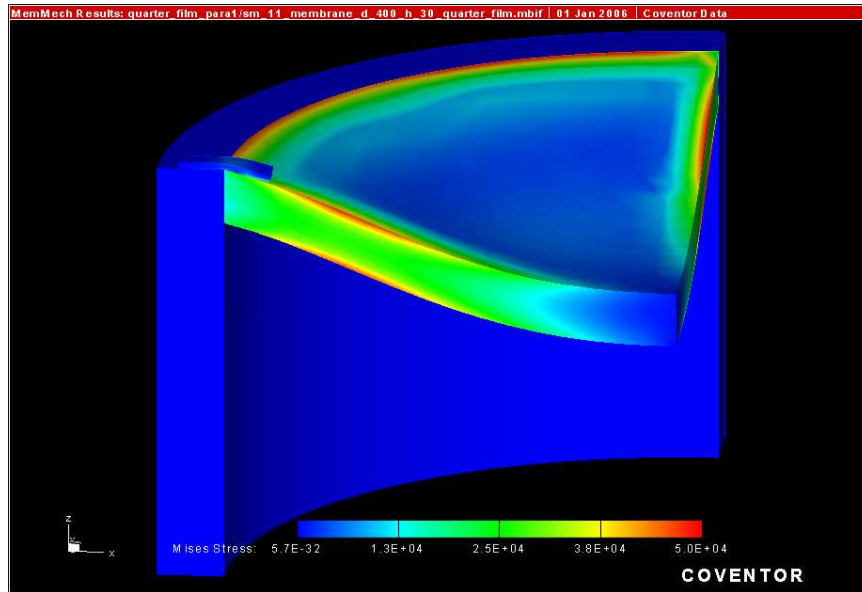
Figure 5.2: Von Mises stress distribution of a clampled circular diaphgram showing how stress is significantly higher along the boundary of the diaphragm and substrate

41

5.2 Surface Characterization

The characterization of device surfaces is very important in MEMS because any superficial defects, roughness, and even differences in thickness could lead to unwanted behavior of the devices. It is also an important step in post-fabrication. As pointed out in Chapter IV, the surface characterization was done using a Zygo interferometer and a surface profiler. A microscope was used to supplement the results obtained.

Figure 5.3 shows the results obtained with the Zygo interferometer. Figure 5.3 (a) is the interferometer's spectrum obtained with a 10X objective from a representative diaphgram in wafer A813. The figure shows areas around the diaphgram where the interferometer was unable to obtain interference patterns. The areas appear as a black ring around the perimeter of the diaphgram. Figure 5.3 (b) is a measurement obtained from the region in the diaphgram where the interference intensity is the highest. The results clearly indicate that the GaN epilayer experienced delamination during fabrication. The reading shows a bulge height of approximately 2 μm. Recall that the film thickness is approximately 4 μm. Figure 5.3 (c) is simply an oblique plot obtained with the intrument's software to show the bulge section and the rest of the diaphgram more clearly.

Micrographs of the front of the diaphgram show that material has been lifted off during fabrication. Figure 5.4 (a) is the top of the diaphgram taken with a 20X objective that clearly shows the areas where material is missing around the perimeter of the diaphgram. Figure 5.4 (b) is a micrograph from an area in the perimeter to show the extent of the damage to the GaN film. The micrograph was taken with a 100X objective. The pictures provide the evidence that material is missing and give an insight to the damage sustained during fabrication. Recall that the fabrication process makes use of a 355-nm laser. Sapphire has a large bandgap (8 eV), which means the laser's energy is passing through to the GaN film where it gets absorbed. Furthermore, because the fabrication of each membrane requires multiple passes in both the x- and y-direction, the film is subject to cumulative effects.
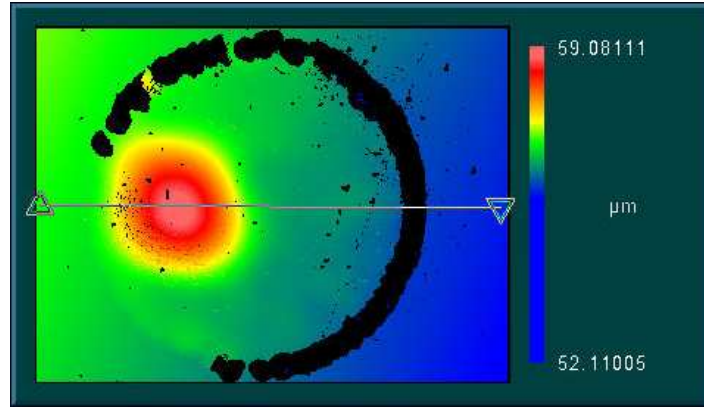
(a)
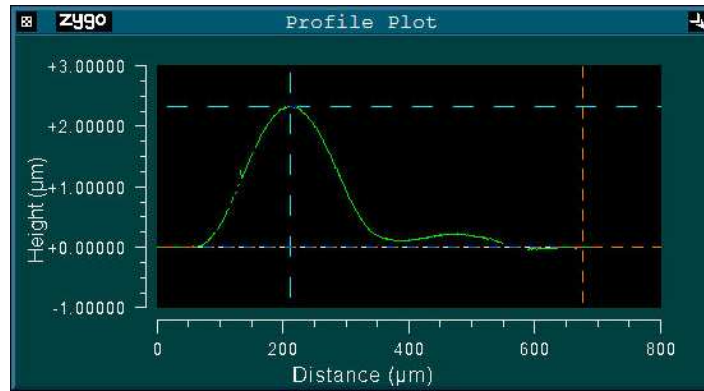
(b)
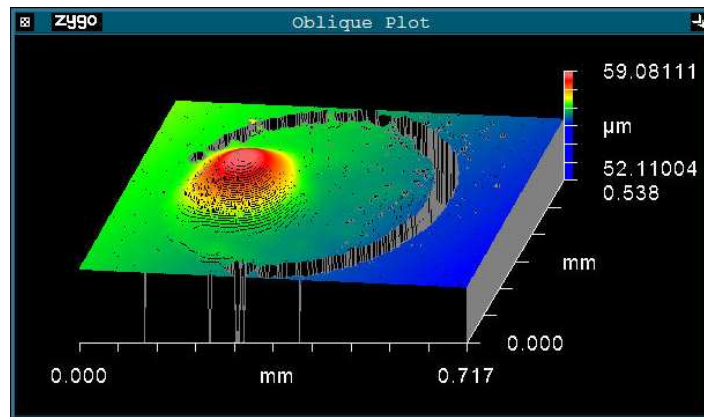
(c)

Figure 5.3: (a) Zygo interferometer spectrum obtained with a 10X objective from a representative fabricated diaphgram. The plot shows areas around the diaphgram where interference could not be obtained. (b) Side profile obtained across the diaphgram where the interference interference is the highest. The height measurement obtained is approximately 2 μm. (c) Oblique construction of the diaphgram that clearly shows the height of the bulge with respect to the rest of the diaphgram.

43

<center>(a)   (b)</center>
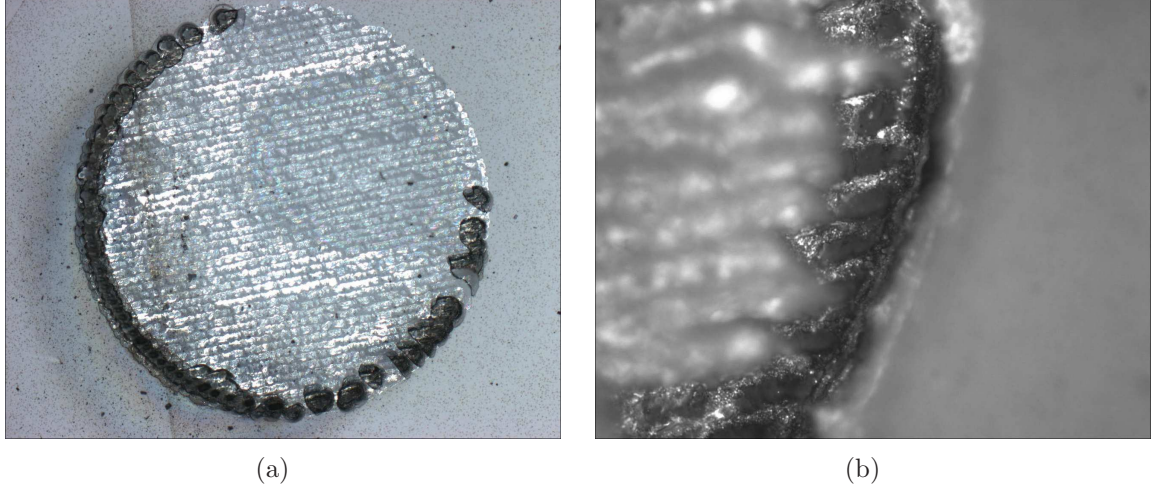
Figure 5.4:   (a) Micrograph of the top surface of a representative fabricated diaph-gram taken with a 20X objective. The picture shows the areas in the perimeter where material is missing. (b) Micrograph of an area in the perimeter of the diaphragm to show the damage extent to the GaN film. The micrograph was taken with a 100X objective.

The Zygo Interferometer results showed the extent of the damage to the GaN epilayer during fabrication. The micrographs presented visual evidence that material is indeed missing around the perimeter of the diaphragms. To further validate the observations, the result obtained with the surface profilometer, and presented in Figure 5.5 (a), show a dip of approximately 4 μm around the perimeter (recall that the GaN film is approximately 4 μm). The figure also shows a 2-μm height on the bulge observed with the Zygo interferometer. Figure 5.5 (b) indicates the location in the diaphragm of the profilometer scan. Figures 5.5 (c) and (d) show the via (on back surface of wafer) and bottom surface of diaphgram, respectively. Both pictures were taken with a 20X objective. The micromachining drilling resulted in a lot of surface roughness as shown in the figure.

5.3   X-ray Diffraction

Omega-theta scans were taken from wafer A813 to qualitatively assess the crys-talline quality of the material. Figure 5.6 shows the results obtained along the wafer.

<center>44</center>
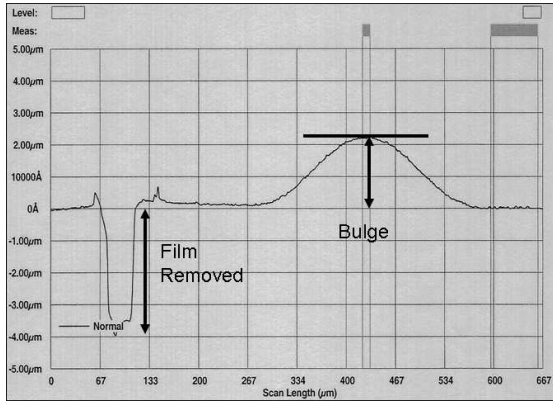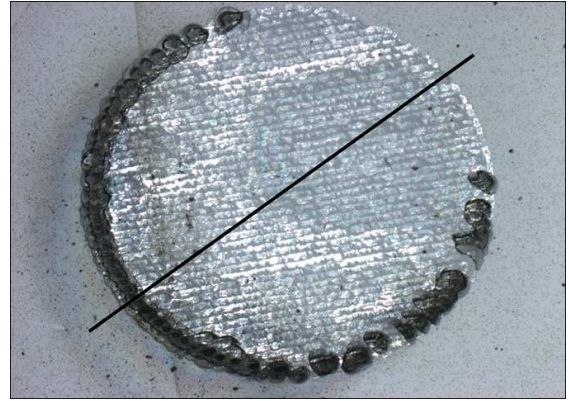
(a)   (b)
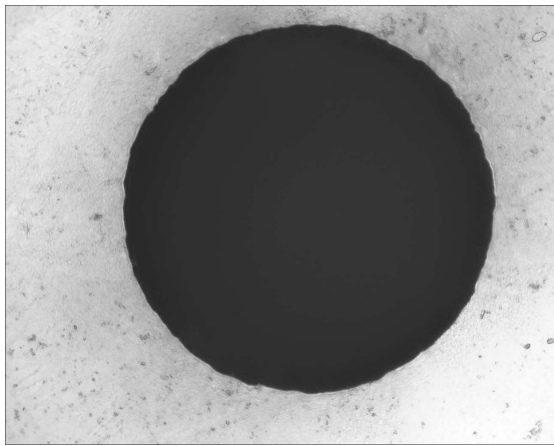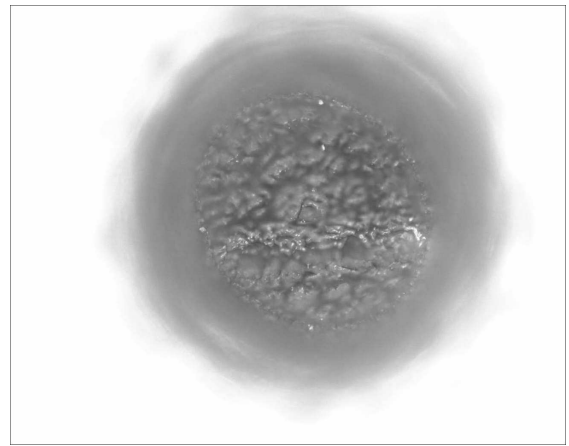
(c)   (d)

Figure 5.5:   (a) Surface profilometer result showing the film lift-off and bulging that occured during fabrication. (b) Picture to show the location of the surface profilometer. (c) Micrograph showing the fabricated via. The picture is from the back surface of the wafer using a 20X objective. (d) Micrograph showing the bottom surface of the diaphragm. The fabrication resulted in a lot of surface roughness on the bottom of the membrane.

The scans were collected at 10, 20, and 30 mm from the center of the wafer along the (002) plane of GaN. The results show that the FWHM increases from the center of the wafer to the outer parts. This behavior indicates that the film quality is not uniform throughout the wafer and confirms the wafer map results shown in Chapter III. XRD can also be used to determine the relaxation of heteroepitaxial films. A reciprocal space map was collected and the results, shown in Figure 5.7, show that the film is relaxed. This can be infered because there is no tilt along the omega axis. However, there is significant broadening of intensity along the omega-theta and omega axes, which indicates a high density of defects in the material. The nature of the defects cannot be accurately determined from this scan.
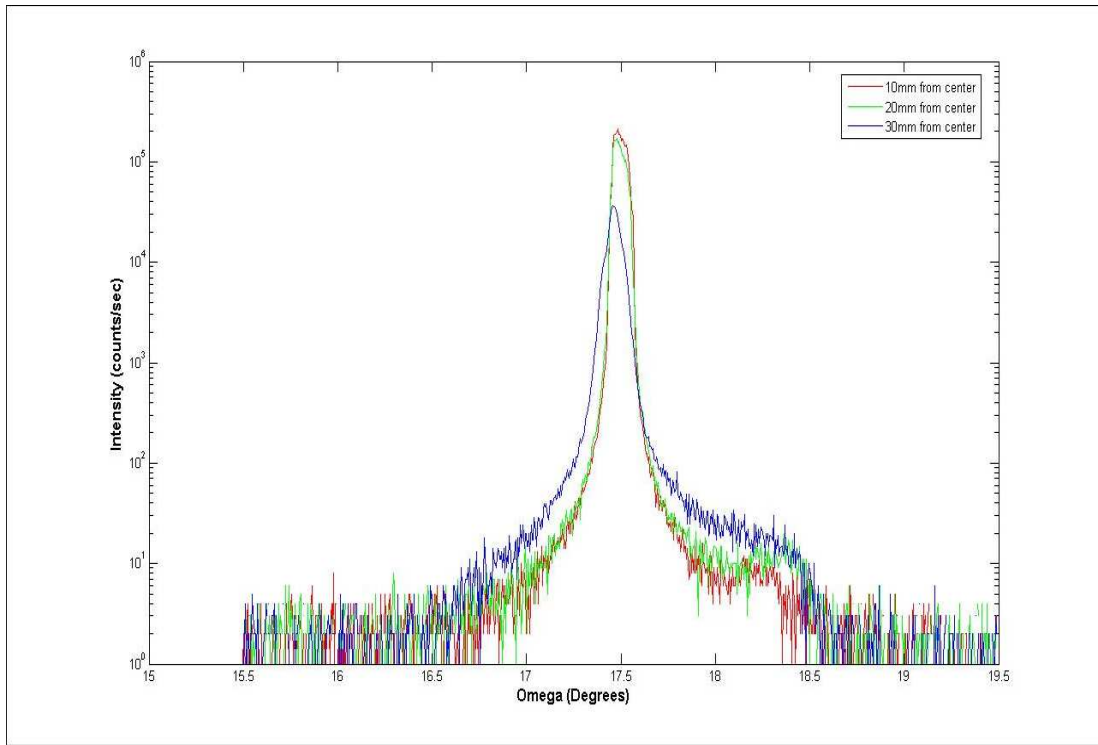
Figure 5.6:   Omega-theta scans of wafer A813 collected to determine the quality of the GaN film throughout the wafer

5.4   μRaman Spectroscopy of GaN on c-plane Sapphire

As pointed out in Chapter II, the use of μRaman spectroscopy has been useful in determining the state of stress in semiconductor materials. In this research, this
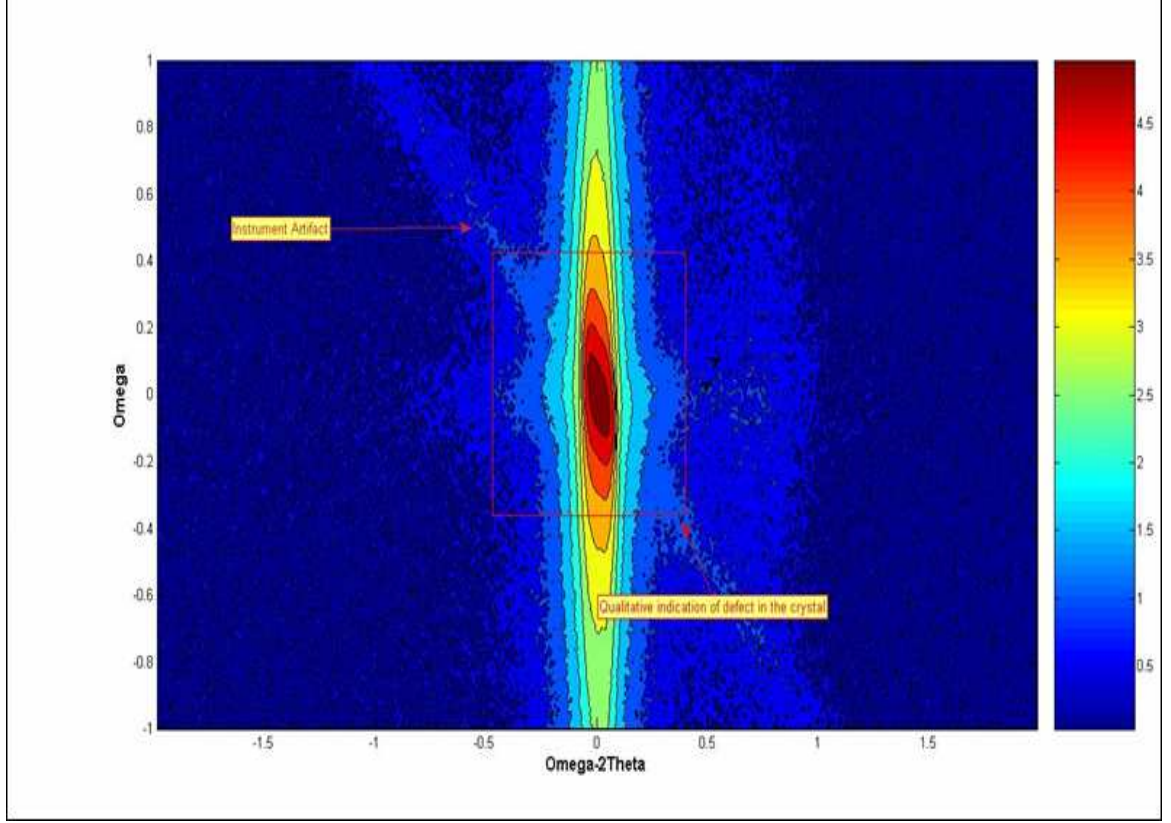
Figure 5.7:   Reciprocal-space map of wafer A813 collected to determine the relaxation of the as-grown film. The film can be assumed relaxed because there is no tilt along the omega axis.

nondestructive technique is primarily used to assess the stress of the circular membranes fabricated using the micromachining laser drilling. The following subsections describe the research performed to meet the objective.

5.4.1 Excitation Source.   To determine the best excitation source to collect the Raman spectra, scans were collected using the 325-, 514-, and 633-nm lasers.

Figure 5.8 shows the results obtained with the three excitation sources. Figure 5.8 (a) shows the scan collected with the 325-nm source. Indicated in the figure are two peaks that cannot be resolved. GaN does not have a phonon frequency around 300 cm^{-1}. The figure also shows a peak at around 750 cm^{-1}, which could correspond to the $A_1(LO)$ or the $E_1(LO)$ phonons [10]. It is, however, difficult to differentiate between the two.

47

Figure 5.8 (b) shows the scan collected with the 514-nm source. The result shows that both GaN and sapphire peaks are measured with this excitation source. It is important to point out that both GaN and sapphire have phonon frequencies at around 750 cm^{-1}. In the figure, that frequency peak is labeled as sapphire, but it could easily be a GaN phonon.

Figure 5.8 (c) shows the scan collected with the 633-nm laser. The scan shows a lot of fluorescence toward the higher frequencies (600 cm^{-1} and above). Sapphire has a phonon frequency at approximately 642 cm^{-1}, but as the scan shows, the peak is very broad. Comparing the three sources, the 514-nm laser appears to provide the best spectra with clearly resolved phonon frequencies of sapphire and GaN.

5.4.2 Instrument Calibration. To determine the accuracy of the instrument, several scans of the internal silicon source were obtained in a span of three months. The scans were collected using the 514- and the 633-nm lasers. However, since it was determined that the 514-nm laser would be the best source of excitation for this research, the accuracy of the instrument was determined using the 514-nm laser source, only.

Renishaw, Inc. specifies that the instrument is able to resolve the silicon phonon peak with an accuracy of 520.5 $\pm$ 0.5 cm^{-1}. Zingarelli had shown that since the peaks in the spectra are statistically fit using a Voigt profile, the mean position of the peak is determined with resolution below the instrument resolution [20]. This is important because the research involves tracking shifts in frequency less than a wavenumber. Statistically, the spectra collected over the three month span give an accuracy of the silicon peak at 520.23 $\pm$ 0.47 cm^{-1}. This is in agreement with the posted accuracy from the company, and it shows that tracking changes in frequency shifts of less than
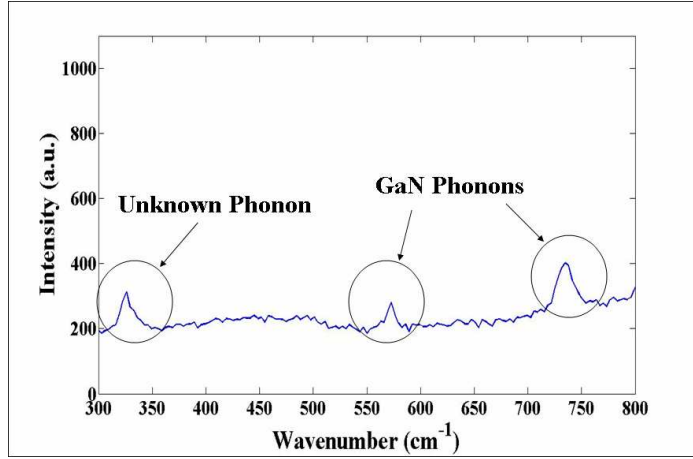
(a)
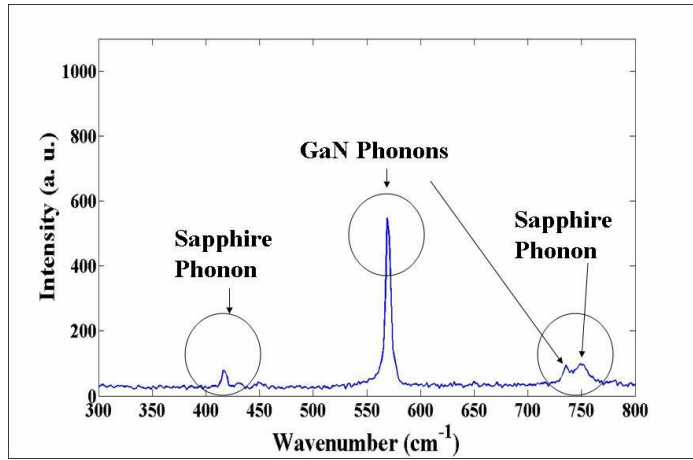
(b)
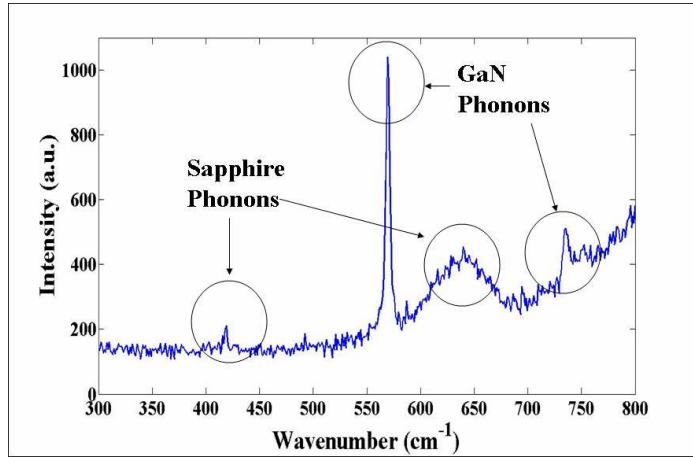
(c)

Figure 5.8: Scans of GaN on c-plane sapphire collected using the (a) 325-nm laser, (b) 514-nm laser, and (c) the 633-nm laser.

49

a wavenumber is possible even though the dynamic sampling rate and spectrometer resolution when using the 514-nm laser are both 2-3 cm^{-1}.

$5.4.3$ *Baseline Spectra.* Figure 5.9 presents the baseline spectra collected from samples A342, A812, A813, and sapphire. The scans were collected at room temperature with the 50X objective to ensure maximum collection efficiency. The purpose of these scans was to characterize the stress of the as-grown material. The scans were collected at a distance far from the fabricated membranes to ensure the influence of the micromachining drilling does not affect the results. Ideally, these scans should have been collected prior to any fabrication process. Unfortunately, the wafers were not available for pre-fabrication analysis. The figure shows that the A_{1g} phonon of sapphire and $E_2(H)$ phonon of GaN are present in samples A342 and A813. Only the $E_2(H)$ phonon is observed in the A812 sample. Notice that the $A_1(LO)$ phonon is clearly observed in sample A342. In the backscatter configuration used, the $A_1(LO)$ phonon is an allowed mode. Therefore, this phonon appears to have shifted to higher wavenumbers in the A813 sample, and it is completely missing in sample A812. The sapphire sample shows all the allowed phonons except the 642 cm^{-1} peak.

$5.4.4$ *Raman Shift as Function of Stress Calibration Using a Four-Point Bending Fixture.* The Raman peak shift as function of applied stress of the $E_2(H)$ phonon of GaN has been experimentally determined in the past by other researchers. Demangeot *et al.* found that the PDP for the case of biaxial stress (ω) in GaN heteroepitaxial film is given by [3].

$$\Delta\omega = 2.43\sigma \ cm^{-1} \tag{5.1}$$

Starman successfully used this technique, of applying strain with a four-point bending fixture, to calibrate the Raman spectrometer so it can be used to detect residual stress in a material [19]. The samples were subjected to compressive strain using the four-point bending fixture. The strain was monitored with the P-3 strain
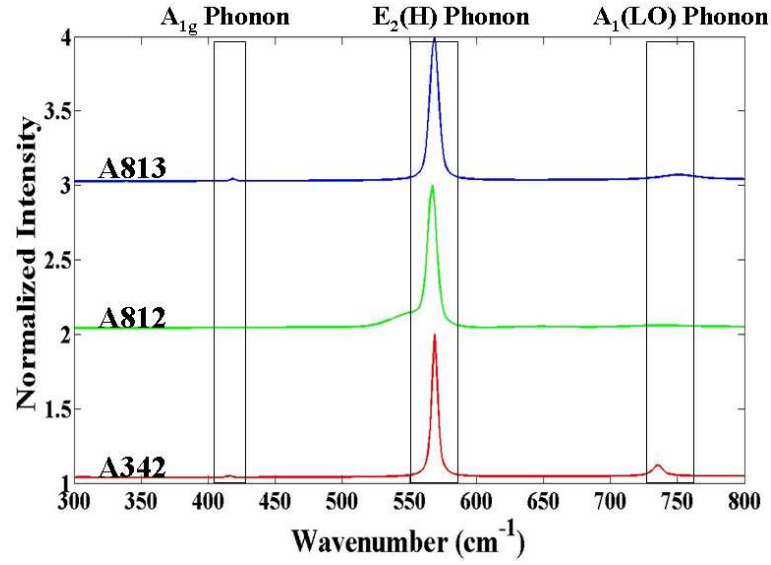
(a)
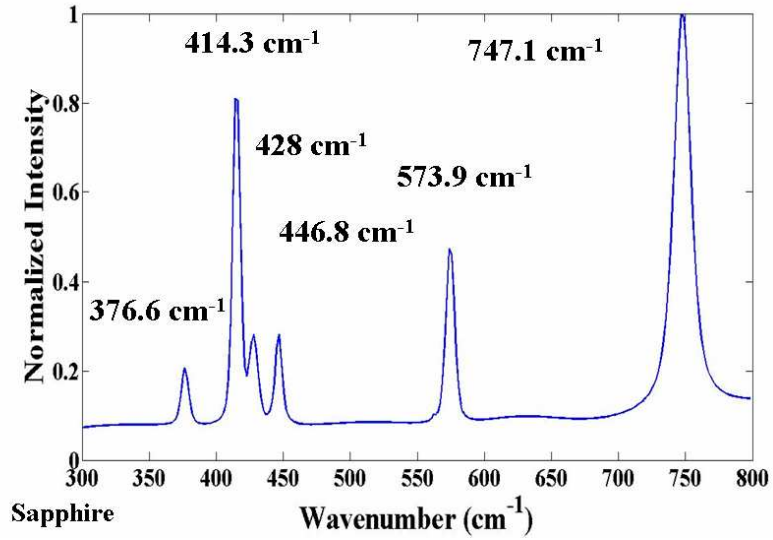
(b)

Figure 5.9: Background spectra of GaN on c-plane sapphire collected using a 50X objective at room temperature in a backscatter configuration from sample (a) A342 (red), A812 (green), A813 (blue), and (b) sapphire. The A_{1g} phonon of sapphire and $E_2(H)$ phonon of GaN are present in samples A342 and A813 but missing in sample A812. Only the $E_2(H)$ phonon is observed in the A812 sample. Notice that the $A_1(LO)$ phonon is clearly observed in sample A342. This phonon is missing in sample A812, and it has shifted to a higher wavenumber in sample A813. The sapphire sample shows all the allowed phonons except the 642 cm^{-1} peak.

indicator. Hooke's law relates strain (ϵ) to stress (σ) in a material by the Young's modulus (E) of the material,

$$\sigma = \epsilon E \tag{5.2}$$

The Raman spectrum corresponding to each strain point was collected using a 20X objective at room temperature. After each strain adjustment, the spectrograph was focused on the surface of the sample to ensure the collection efficiency of the objective would remain the same. The fitting was done using a linear, robust bisquare fitting algorithm using the code contained in Appendix C. A bisquare fitting method minimizes the summed square of the residuals and minimizes the effect outliers have on the overall fit. It is a more robust method than a simple linear least square method.

Figure 5.10 shows the linear fit obtained for the E_2 phonon of GaN. From the linear fit, Raman shift as a function of stress in GaN film is given by equation (5.3). The slope of the equation is given in units of cm^{-1}/GPa.

$$\nu_{E_2 H} = 0.2051\sigma + 568.5 \; cm^{-1} \tag{5.3}$$

Even though a fit was obtained, the peak shift is not appreciable considering the amount of compressive stress applied to the sample. The peak shifts, as function of applied stress, can be tracked even at the low resolution and dynamic sampling rate of the instrument because of the nonlinear fit performed on the data. The resolution affects the broadening of the peak, but the peak can be tracked to shifts of less than a one wavenumber. Figure 5.10, however, shows a range of approximately 0.5 cm^{-1}, which is less than the standard deviation ($s_y = 0.4342 \; cm^{-1}$). So even though the fitting performed has some statistical merit because the standard error of the estimate ($s_{y/x} = 0.3730 \; cm^{-1}$) given by [2],

$$s_{y/x} = \sqrt{\frac{sse^2}{n-2}} \tag{5.4}$$
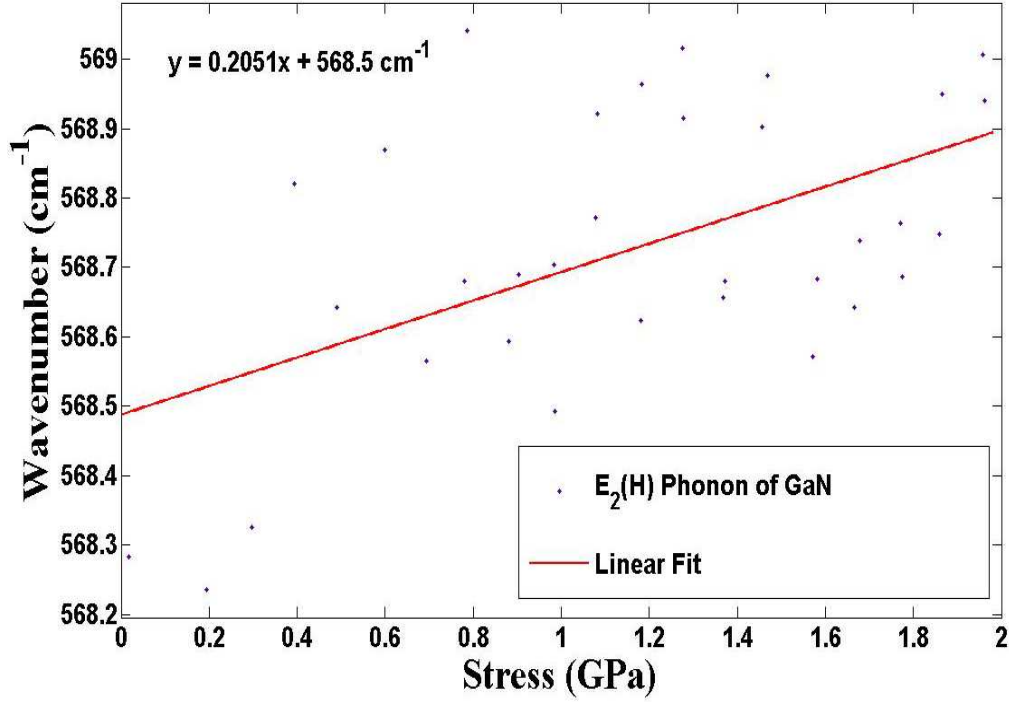
Figure 5.10:   Linear fit of the $E_2(H)$ phonon of GaN obtained using a linear, robust bisquare fitting algorithm. Strain was applied to the sample using a four-point bending fixture and monitored using a P-3 strain indicator

where sse is the square of the sum of the error, and n is the number of data point, is less than the standard deviation, the data does not yield enough statistical confidence to accurately claim the fit obtained represents the PDP of MBE-grown GaN.

The experimental value for GaN obtained in this research differs by one order of magnitude from the one obtained by Demangeot *et al.* The difference can be attributed to the experimental technique used to determine the deformation potentials. In this bending technique (four-point bending fixture), the sample under examination experiences the largest moment between the two center contact points (refer to Figure 4.5). The initial assumptions were that the interface between the plexiglass beam and sample of GaN on sapphire was ideal (thus making it a trilayer structure consisting of plexiglass, sapphire and GaN epilayer), and that the sample experienced pure bending (thus the moment was considered constant between the two center points). The

entire structure (plexiglass and sample) was assumed to be one, which meant the top surface (the GaN epilayer) would experience compression while the bottom surface (the bottom of the plexiglass beam) would be under tension. This is consistent with pure bending of beams. In this case, stress (σ) is directly proportional to the moment. The problem, however, is that all three materials have different Young's moduli thus rendering the initial assumptions wrong. The GaN epilayer does not appear to compress during the bending, and the data obtained does not support the assumptions. Also, Demangeot *et al.* experimented on wurtzite GaN grown on (111) silicon rather than sapphire. Recall that sapphire poses the highest lattice constant mismatch of all the substrates available for GaN heteroepitaxial film growth.

Figure 5.4.4 shows the linear fit for the A_{1g} phonon of sapphire. From the linear fit, Raman shift as a function of stress in sapphire is given by equation (5.5). The slope of the equation is given in units of cm^{-1}/GPa.

$$\nu_{A_{1g}} = 0.152\sigma + 417 \ cm^{-1} \qquad (5.5)$$

This research constitutes the first attempt at determining the phonon deformation potential for sapphire. The frequency shift as function of stress was minimal (less than a wavenumber). The standard deviation of the data was $s_y = 0.2071 \ cm^{-1}$, while the standard error of the estimate, as given by equation stderror, is $s_{y/x} = 0.3023 \ cm^{-1}$. There is not statistical merit in these results because $s_{y/x}$ is higher than s_y [2].

As previously mentioned for GaN, the data obtained cannot be attributed to the strain applied with the four-point bending fixture. The conclusion drawn for the GaN epilayer can be drawn for sapphire.

One more possibility that can be considered is that the bond used to fix the sample onto the plexiglass beam relaxed, thus preventing the sample from bending with the plexiglass beam.
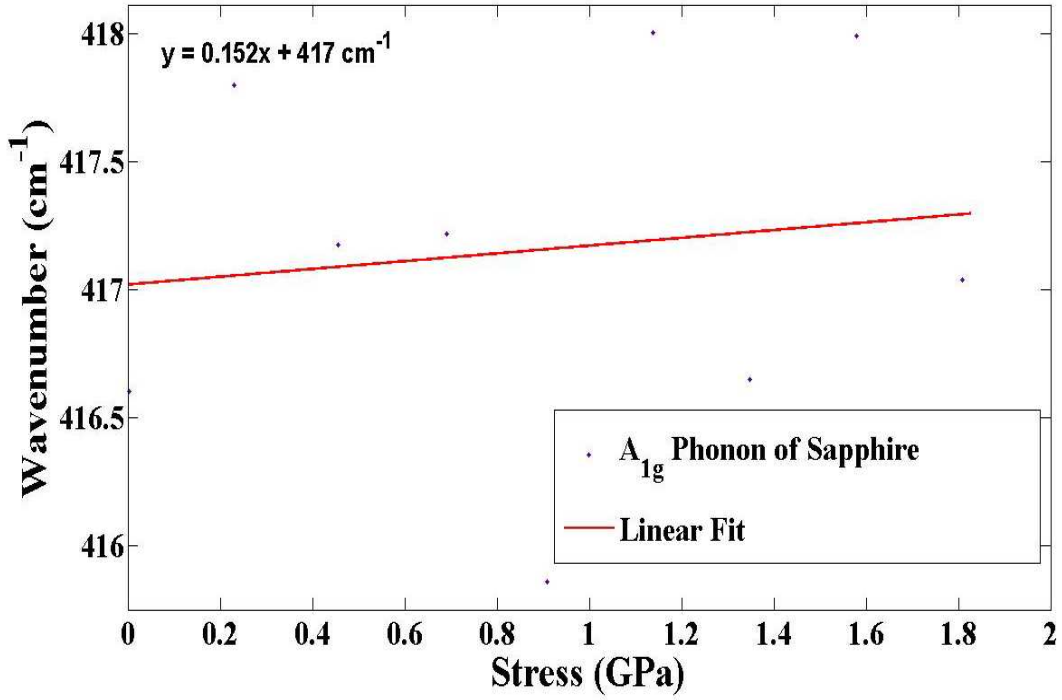
Figure 5.11:　Linear fit of the A_{1g} phonon of GaN obtained using a linear, robust bisquare fitting algorithm. Strain was applied to the sample using a four-point bending fixture and monitored using a P-3 strain indicator

5.4.5　Stress Characterization of Fabricated Membranes.　Since the PDP determination for both GaN and sapphire failed to provide a reliable linear fit of peak shifts as function of applied stress, the GaN PDP obtained by Demangeot *et al.* was used to characterize the state of stress of the fabricated membranes.

Line scans across the membranes and raster scans that overlap the boundary between the membrane and the substrate are useful in determining the stress. A series of line and raster scans were collected from a representative membrane in each of the wafers A812 and A813 for the purpose of mapping out the stress state. The scans were fit with a nonlinear Voigt profile using the code included in Appendix C and the InVia accompanying software Wire 2.0.

5.4.5.1　Line Scans.　Figure 5.12 presents the results obtained from three line scans collected along the radius of membrane 1 in wafer A812. The scans

were collected in steps of 10 μm at room temperature using the 50X objective, 100% laser power on the sample (6.30 mW). The stress across the membrane is calculated using equation (5.1). The plot shows that the stress across the membrane is mostly compressive, as expected, because of the lattice mismatch between wurtzite GaN and sapphire. The errorbars in the plot were calculated using the standard deviation specified in equation GaNpdp$_d$$emangeot$1001[3].

Figure 5.12: Residual stress distribution along the radius of membrane 1 in wafer A812. The stress was mapped using the PDP found by Demangeot *et al.*

Figure 5.13 shows the stress result along the radius of membrane B in wafer A813. The scans were collected with the same conditions of results shown in Figure 5.12. Similarly to membrane 1 of wafer A812, the stress is compressive in nature.

The state of stress determined in this research represents the residual stress in the material post-fabrication. As stated before, the laser used during fabrication may cause localized heating of the sapphire and consequently the film, which may result in

Figure 5.13: Residual stress distribution along the radius of membrane B in wafer A813. The stress was mapped using the PDP found by Demangeot *et al*

.

stress changes in the material. Sapphire has a very poor thermal conductivity, thus rendering it a very ineffective heat sink [11].

5.4.5.2 Raster Scans. Raster scans along the boundary of the fabricated membrane and substrate were collected for the same membranes characterized with the line scans. The raster scans are useful because they directly pinpoint to areas where stress is high. The scans are plotted as function of position and position references are provided for ease of understanding.

GaN Film. For comparison, the raster scans for membranes 1 (A812) and B (A813) are provided in Figures 5.14 (a) and (b). The overall stress in membrane 1, wafer A812 is less than the membrane B, wafer A813. The figures show how the state of stress is not uniform on either side of the membranes, and it also gives

evidence that stress is higher inside the membrane. Furthermore, the boundary line is characterized by the highest level of stress. This is in accordance with the behavior expected for a clamped, circular membrane. The same results were observed in the FEA modeling results. It is important that stress be evenly distributed along the boundary so the response of the piezoresistive elements overlapping the membrane and substrate can be accurately predicted, and even though the figure shows a difference in stress in and outside the membrane, the results do not provide that even distribution sought.

(a)

(b)

(c)

(d)

Figure 5.14:   Raster scan setup showing the 10000-μm^2 grid used for the scan of wafers (a) A812 and (b) A813. The scans were collected at every 10 μm. Raster scan of (c) membrane 1, wafer A812, and (d) membrane B, wafer A813.

The linewidth of the $E_2(H)$ phonon varies with position as well. Good quality material has a linewidth of approximately 3 cm^{-1} [11]. This distribution shows that the film quality varies in small spatial positions in both the membrane and outside the

membrane. Figure 5.15 highlights how the Raman peak, as well as the linewidth, vary with position for both membranes 1 and B, wafers A812 and A813, respectively. In Figures 5.15 (a) and (b), the maps show a 2-cm^{-1} span ranging from 566-568 cm^{-1} for membrane 1, wafer A812, and 567-569 cm^{-1} for membrane B, wafer A813. Fabrication of the membrane results in significant damage to the GaN film. The absorption of the laser energy during fabrication drastically changes the Raman spectra of the GaN film. For instance, the linewidth in the middle of wafer A813 (far away from any fabricated membrane) is approximately 1.5 cm^{-1}. In contrast, the linewidth in the middle of the membrane is 3.4 cm^{-1} while just outside the membrane is 2.73 cm^{-1}. The three values clearly differ from the 3-cm^{-1} linewidth considered to be quality film [11]. These two values, although close to the 3 cm^{-1} linewidth mentioned as quality film, differ significantly from the value obtained in the middle of wafer A813. This difference confirms the damage sustained by the film during fabrication.

Figure 5.16 shows the spectra obtained in the middle of the membrane, as well as just outside the membrane, to show the effect the fabrication had on the film. Notice, for instance, how the $A_1(TO)$ phonon of GaN appears after fabrication. The baseline spectra of wafers A812 and A813 (Figures 5.9 (a) and (b)) did not show this peak, which leads to the conclusion that the thermodynamic effects of the micromachining drilling resulted in the appearance of this peak.

Sapphire. The PDP of sapphire is not statistically reliable. The Raman peak distribution, however, can be used as an indicator of the changes in the material post fabrication. Figure 5.17 shows the wavenumber shift across the boundary of the membrane. The plots shows a 10-cm^{-1} range, which is quite large but necessary to show the variation obtained. In the plots, the sections that appear white indicate areas where the A_{1g} phonon could not be detected. This behavior cannot be explained and further testing needs to be accomplished to determine if the sapphire substrate sustained enough damage to prevent the detection of the phonon. In Figure 5.17 (d), the A_{1g} distribution is fairly uniform outside the membrane with

Figure 5.15: (a) $E_2(H)$ Raman peak distribution used to determine the stress in (a) membrane 1, wafer A812, and (b) membrane B, wafer A813, shown in Figure 5.14. Linewidth of the $E_2(H)$ Raman peak showing the quality of the GaN film in (c) membrane 1, wafer A812, and (d) membrane 1, wafer A812.

values averaging between 417 to 418 cm^{-1}. On the other hand, Figure 5.17 (c) shows a wider distribution of peak shifts. Figure 5.16 showed the effect fabrication had on the Raman spectra; notice, for instance, how the intensity of the A_{1g} phonon has significantly dropped after fabrication. This could be the reason why inside the membrane it is difficult to detect it; however, it does not explain those areas outside the membrane.

5.5 Summary

The results presented show that the fabrication process introduces significant damage to the GaN film and the sapphire. The surface characterization conclusively

Figure 5.16: Comparison of spectra inside and outside of membrane B, wafer A813 to show the appearance of the $A_1(TO)$ of GaN after fabrication.

serves as evidence of the damaging effect the laser energy. Raman spectroscopy results point to the changes in film quality using the linewidth of the $E_2(H)$ phonon of GaN as the indicator. Determining the PDP of GaN and sapphire experimentally using the four-point bending fixture was unsuccessful because the peak shifts induced could not be attributed to applied strain. The state of stress distribution of the GaN epilayer in representative membranes of wafers A812 and A813 was mapped using the PDP obtained by Demangeot *et al.* For sapphire, the Raman peak shifts were mapped to make the correlation between stress and peak shifts.

(a)   (b)

(c)   (d)
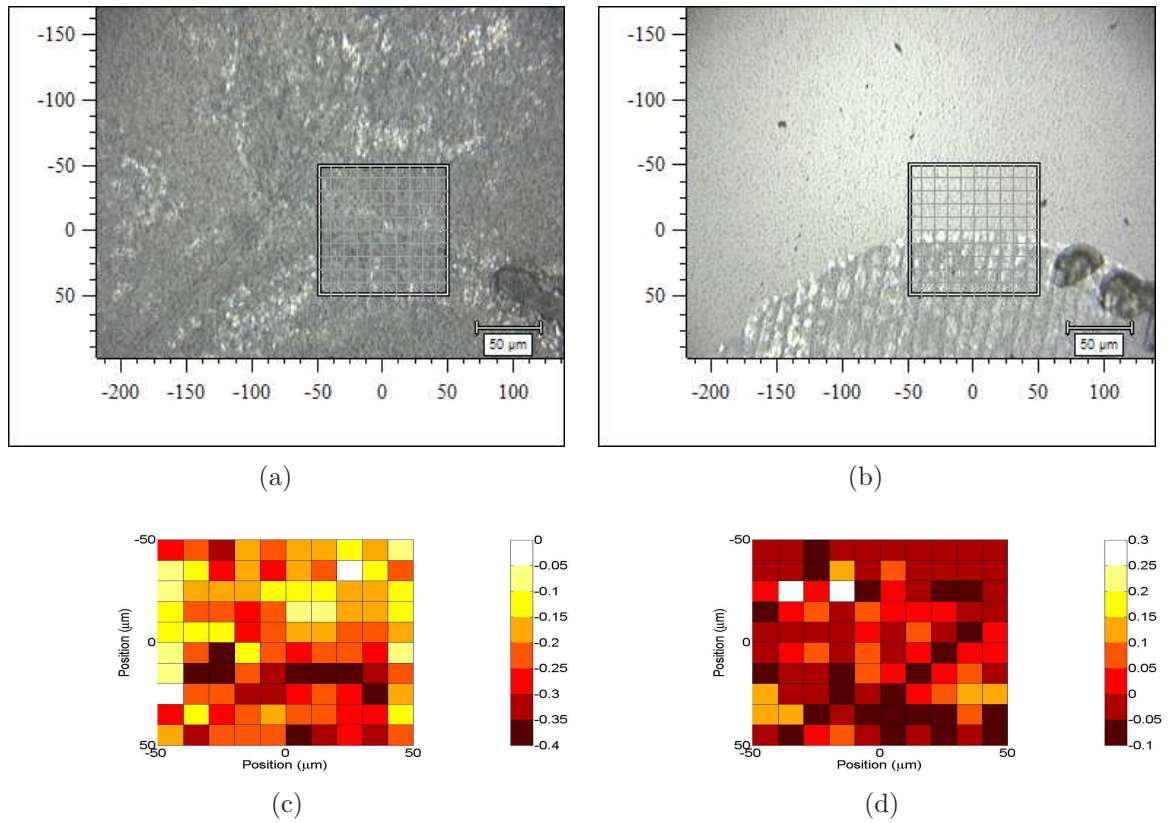
Figure 5.17:   Raster scan setup showing the 10000-μm^2 grid used for the scan of wafers (a) A812 and (b) A813. The scans were collected at every 10 μm. Sapphire A_{1g} phonon map distribution for (c) membrane 1, wafer A812 and (d) membrane 1, wafer A813. The maps show areas where the phonon could not be detected.

62

VI. Conclusions and Recommendations

μRaman spectroscopy has been in use since the early 1970's to examine the state of stress in semiconductor materials. It is a proven, nondestructive technique, capable of detecting areas of high residual stress through the PDP, which relates the Raman peak shift to stress. Determining the PDP for both GaN and sapphire was experimentally attempted but did not yield useful results. Line and raster scans were collected to characterize the stress in the circular membranes fabricated with the novel laser micromachining drilling technology. Surface characterization techniques, XRD, and FEA were performed to supplement the μRaman spectroscopy.

6.1 Conclusions

The reliability of MEMS devices starts with material selection, but more importantly, with knowing the type of environment under which it will be operated. WBG materials are quickly fulfilling the role that silicon-based devices dominated for years. SiC proved to be an excellent candidate for the fabrication of the MEMS micro-pressure sensors under the Generation-After-Next munitions program. It is well characterized and growth/fabrication processes are improving. GaN has gained ground with the advent of blue-emitting diodes and other devices that operate in the ultra-violet regime. Fabrication of GaN-based MEMS must improve for the material to remain a suitable candidate for operation in harsh environments. The results obtained in this research prove that laser micromachining drilling with the 355-nm laser introduces significant damage to both the heteroepitaxial GaN film and the sapphire substrate. Understanding the physical process that occurs during laser drilling is critical in order to assess the damage it imposes on the material. Laser drilling is, in fact, a violent process in which the material melts, ablates, and then cools down to the solid state again. Now, the suitability of a particular laser for the fabrication must account for these factors.

μRaman spectroscopy results showed the state of stress of the fabrication membranes. Unfortunately, there are not any suitable fabrication procedures (wet etching,

deep reactive ion etching, *etc.*) that could quickly produce sapphire circular membranes for micro-pressure sensors.

Determining the PDP for GaN on c-plane sapphire proved difficult because of the inability to exert any significant strain using the four-point bending fixture. However, this research effort represents the first time this Raman shift as function of stress in sapphire has been attempted.

6.2 Recommendations for Future Work

Further analysis of the damage to the film and substrate is needed to fully understand the effect of the laser used for fabrication. The extent of the damage in the material could be directly related to the absorption of the energy by the material (heating of the material). A study of how the material properties, such as thermal conductivity and heat capacity, behave in response to the rapid heating due to the incident laser energy is paramount. Any future research should include analyzing the wafers prior to fabrication using XRD and μRaman spectroscopy in order to have a baseline characterization of the material.

To aid in the PDP determination, thinning of the material could be explored. Sapphire wafers can be thinned to about 10 μm and are readily available in the commercial sector. Thin samples can then be used with the four-point bending fixture to find the relationship between stress and Raman peak shift. Thinned sapphire samples (approximately 7.5 centimeters (cm) long by 1 cm wide by 150 μm thick) were ordered from a commercial vendor and should be tested once available.

Laser Mounds and Photonic Center, Inc., will explore using a different wavelength laser for the fabrication of the membranes. As mentioned above, a baseline analysis of the wafers pre-fabrication must be accomplished on the wafers to examine the effect this new laser will have on the material.

Appendix A. Analytical Modeling of MEMS Micropressure Sensors

The sensing element in a micromachined mechanical transducers relies on material properties that include piezoresistivity, piezoelectricity, capacitance, and others. The type of microsensor discussed in this thesis uses the piezoresistive property of wide bandgap semiconductor materials. Piezoresistive is a term with greek roots; piezin means "to press." Some materials experience a change in resistivity when a pressure is impinged on them. The piezoresistive elements in this type of transducer are usually arranged in a Wheatstone bridge configuration. The measured and supplied voltage to the Wheatstone bridge is given by

$$V_{out} = V_{in} \left(\frac{R_1}{R_1 + R_4} \right) \tag{A.1}$$

Where $\mathbf{V_{out}}$ and $\mathbf{V_{in}}$ are the measured and supplied voltage to the Wheatstone bridge circuit, respectively.

Usually, the mechanical structure that is used for sensing is a diaphragm. Diaphragms can be either circular or rectangular. This appendix describes the analytical equations that describe the operation of a circular diaphragm that is rigidly clamped [1]. Usually, MEMS fabrication techniques do not yield simply supported structures. The analysis is only valid under the following assumptions:

- The diaphragm is flat and uniform.

- The material is homogeneous and isotropic.

- Pressure is applied normally to the plane.

- The elastic limit of the material is not exceeded.

- The diaphragm is not too thick.

- deformation is due to bending and the neutral axis experiences no stress.

Figure A.1 depicts a rigidly clamped diaphragm and its associated deflection under uniform pressure load. Note that in the figure the rigidity of the edges has

been exagerated for illustration purposes. It is important to point out that pressure P can be applied to either side of the membrane. Bedises deflection, this type of structure can be characterized by its stress distribution; the two stress components are radial and tangential.

Figure A.1: Side view of a rigidly clamped circular diaphragm and its displacement under a uniform pressure load. P is the applied pressure, a is the radius of the diaphragm and r is the radial distance.

The deflection y at a radial distance r under uniform pressure load P for a rigidly clamped structure, as shown in Figure A.1, is given by equation (A.2)).

$$y = \frac{3(1-\nu^2)P}{16Eh^3}\left(a^2 - r^2\right)^2 \qquad (A.2)$$

Where **h** is the thickness, **E** and ν are the Young's modulus and Poisson's ratio, respectively, and **a** is the radius of the diaphragm.

As mentioned above, the other characterizing elements are both the radial and tangential stress distributions across the diaphragm. The neutral axis depicted in A.1 experiences zero stress while the outer faces suffer from maximum stress. The two stress components are given by equation (A.3). Equation (A.3a) governs the radial stress, σ_r, while equation (A.3b) describes the tangential stress, σ_t.

$$\sigma_r \;=\; \frac{3}{8}\frac{Pa^2}{h^2}\left[(3+\nu)\frac{r^2}{a^2} - (1-\nu)\right] \tag{A.3a}$$

$$\sigma_t \;=\; \frac{3}{8}\frac{Pa^2}{h^2}\left[(3\nu+1)\frac{r^2}{a^2} - (1-\nu)\right] \tag{A.3b}$$
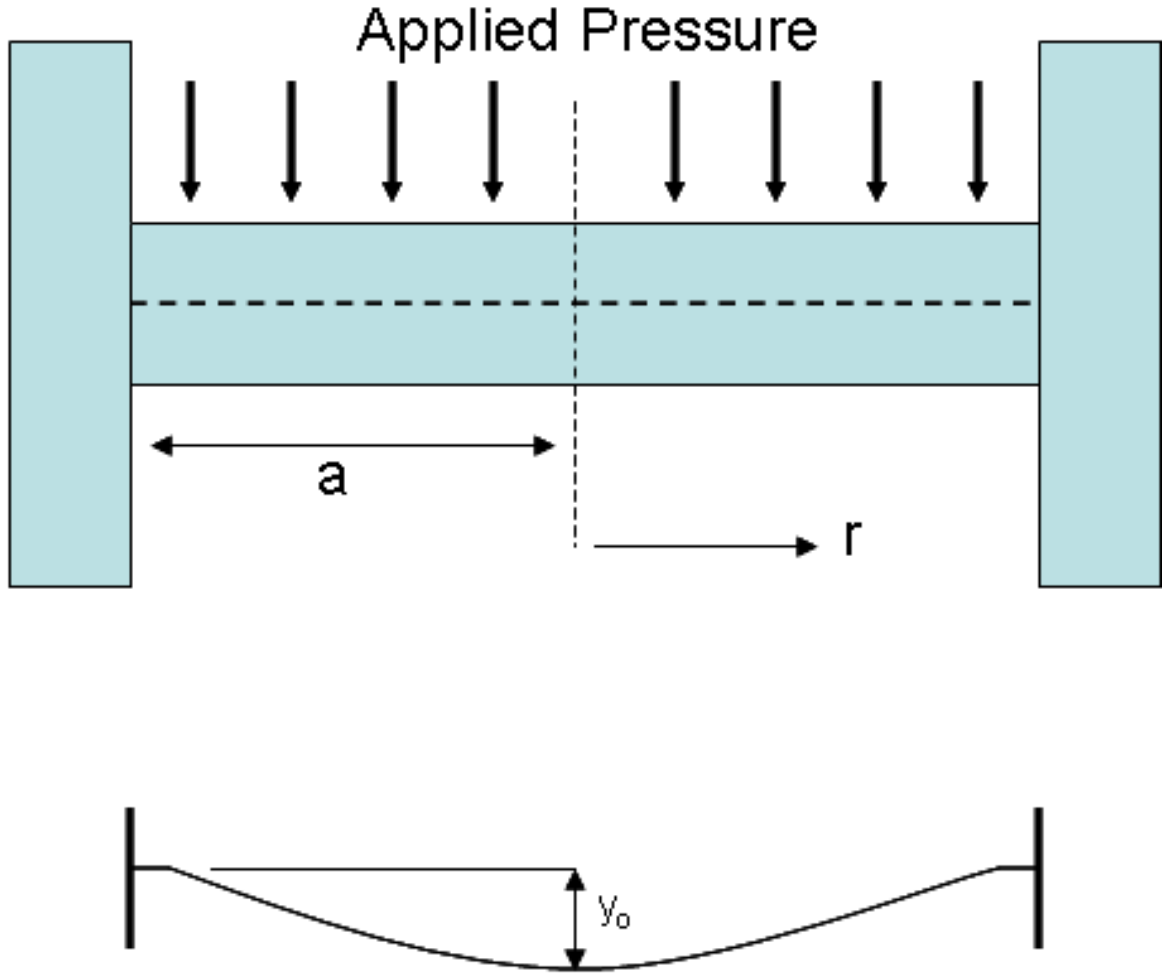
Appendix B. Renishaw Specifications

These are the specifications of the Renishaw InVia spectrometer obtained from AFRL/MLBP.

Technical Specifications
For The
Renishaw in Via Raman Microscope

Location: AFRL Building 655, Room 139
Date: 3/17/2005

Lasers:

Manufacturer	Wavelength (nm)	Type	Power (mW)	Polarization Ratio
Kimmon	325	HeCd	200	500:1 (vertical)
Melles Griot	514.5	Argon Ion	150	250:1 (vertical)
Renishaw	632.8	HeNe	30	500:1 (vertical)
Renishaw	830	Diode	300	N/A

Microscope Objectives:

Name/Type	NA	Working Distance (mm)	Efficiency
x5	0.12	14.0	0.02
x20	0.40	0.39	0.25
x50	0.75	0.37	1.00
x50 LWD	0.50	10.6	0.40
x15 NUV	0.32	8.50	0.16
x40	0.50	1.00	0.40

Notes:
  NA=numerical aperture
  Efficiency=estimation of collection efficiency relative to standard x50 objective
  LWD=long working distance
  NUV=near ultraviolet

Spot Size (in μm):

Objective \ Wavelength	325nm	514nm	633nm	830nm
x5	N/A	2.61	3.22	4.22
x20	N/A	0.78	0.97	1.27
x50	N/A	0.42	0.52	0.68
x50 LWD	N/A	0.63	0.77	1.01
x15 NUV	0.62	N/A	N/A	N/A
x40 NUV	0.40	N/A	N/A	N/A

Laser Power on Sample (mW):

Objective \ Wavelength	325nm	514nm	633nm	830nm
x5	N/A	7.30	1.20	103
x20	N/A	7.50	1.30	106
x50	N/A	6.30	0.68	88
x50 LWD	N/A	4.80	0.11	55

Grating Scan Wavenumber Resolution (cm⁻¹):

Grating \ Wavelength	325nm	514nm	633nm	830nm
1200 lines/mm	N/A	~4-5	~2-3	~1
1800 lines/mm	N/A	~2	~1	N/A
2400 lines/mm	~2-3	N/A	N/A	N/A

*Imaging band pass filters have a 15-20 wavenumber pass band.

(a)

(b)

Appendix C. Renishaw Specifications

C.1 Voigt Fitting Algorithm

Program used to fit the Raman spectra using a nonlinear Voigt profile algorithm.

Listing C.1:   Voigt Fitting Algorithm. (Appendix3/Raman.m)

```
%*****************************************************************************...

% Micro-Raman Data Analysis Program (MRDAP)
%*****************************************************************************...

% Version 2.00
% Date: 23 December 2005

% Changes:
%    (1) Removed the selection of reference files

% Suggested future changes:
%    (1) Use NARGIN to allow script-like/batch execution of a list ...
     of files.
%    (2) Same as (1), but to initialize the GUI default directory ...
     instead.

% Authors: Jason Foley(1), Capt Frank Parada (2), and Michael ...
     Marciniak (2)
%            (1) AFRL/MNMF, jason.foley@eglin.af.mil, (850)...
     883-0584
%            (2) AFIT/ENG, michael.marciniak@afit.edu, (937)...
     255-3636 x 4529

% Description:
%    This program processes the spectral data in micro-Raman data ...
     files from
%    a Renishaw machine.  The data is written to a "summary" file, ...
     with
%    point-by-point values for all of the tracked peaks.  The peaks...
      are
%    summarized in the
%
% Pseudocode:
%    1. File Import and Data Extraction
%    2. Sampling Plot
%    3. Curve fitting
%         a. Gaussian + Lorentzian = Voigt!

% References:
%    [1] Timucin, Dogan A., 2004, "A new computational framework ...
     for
%        atmospheric and surface remote sensing," Proc. ESTC 2004, ...
     B9P1,
```

69

```matlab
%          pp. 1-7.
%     [2] Puerta , Julio , and Martin , Pablo , 1981 , "Three and four
%          generalized Lorentzian approximations for the Voigt
%          line shape ," Appl. Opt., 20 (22) , pp. 3923-3928.
%     [3] Foley , Jason R., et al., 2006 , "Data reduction for micro -...
   Raman
%          spectroscopy experiments ," in preparation for submission ...
   to J.
%          Raman Spectroscopy.
%
%function [linek0]=Raman
function main()
%% Setup
dbstop if error
clc;
clear all;
figure(1);
clf;

%% File Import GUI

% File selection for data importation (GUI Codelet)
cd('C:\Documents and Settings\Frank\My Documents\Thesis Folder\...
   Processed Raman Data\19Oct05');
% Begin GUI codelet to select the SCAN DATA files for analysis
dirchange = true;
while dirchange
    % dialog for file name
    currdir = cd;
    d = dir;
    str = {d.name};
    isdir = [d.isdir];
    dirindices = find(isdir == true);
    dialogstr = str;
    for ii = 1:length(dirindices)
        dialogstr(dirindices(ii)) = {['<',char(str(dirindices(ii))...
            )),'>']};
    end
    % select SCAN data files (allow multiple files)
    [s,v] = listdlg('PromptString','Select SCAN data file(s):',...
        'SelectionMode','multiple',...
        'ListString',dialogstr);
    if strcmp( '..',char(str(s)))
        % Chosen is directory... want to go up a level
        lastslash = max(findstr(currdir,'\'));
        currdir(lastslash+1:end) = [];
        cd(currdir);
    elseif strcmp( '.',char(str(s)))
        % Chosen is directory... want to refresh current directory...
             ... just
        % don't allow anything to happen, as it will repopulate at
        % beginning of while loop
```

```matlab
        elseif isdir(s)
            % Chosen is subdirectory... append to current path and ...
                start over
            currdir = [currdir,'\',char(str(s))];
            cd(currdir);
    else
            dirchange = false;
        end
    end

% Read in data file(s)
    Ndf = length(s); % number of data files
    Nscans = zeros(Ndf,1); % total number of scan locations
    for idf = 1:Ndf
        filename{idf} = d(s(idf)).name;
        disp(sprintf('Scan data file selected: %s.',filename{idf}));
        % Open the file
        filedata{idf} = importdata(filename{idf});
        [nrows,ncols] = size(filedata{idf});
        switch ncols
            case 2
                % Point scan
                xi{idf} = 0;
                Nx(idf) = length(xi{idf});
                %
                yi{idf} = 0;
                Ny(idf) = length(yi{idf});
                %
                scantype{idf} = 'point';
                Nscans(idf,1) = 1;
                kcol = 1; % column with k values
                Scol = 2; % column with S values
            case 4
                % Find the unique locations... X
                xi{idf} = unique(filedata{idf}(end:-1:1,1));
                Nx(idf) = length(xi{idf});
                % and Y
                yi{idf} = unique(filedata{idf}(end:-1:1,2));
                Ny(idf) = length(yi{idf});
                % Assemble the knowledge
                if Nx(idf) == 1
                    % A vertical line
                    scantype{idf} = 'yline';
                    Nscans(idf,1) = Ny(idf);
                elseif Ny(idf) == 1
                    % A horizontal line
                    scantype{idf} = 'xline';
                    Nscans(idf,1) = Nx(idf);
                else
                    % Area scan (raster, circle, or other)
                    scantype{idf} = 'area';
                    Nscans(idf,1) = Ny(idf)*Nx(idf);
```

```
                    end
                kcol = 3; % column with k values
                Scol = 4; % column with S values
135     end

        % Sort the x and y vectors...
        ixy = 1;
        for iy = 1:Ny(idf)
140         for ix = 1:Nx(idf)
                x{idf,ixy} = xi{idf}(ix,1);
                y{idf,ixy} = yi{idf}(iy,1);
                ixy = ixy + 1;
            end
145     end

        % Sort the signal and wavenumber vectors...
        Nk = nrows/Nscans(idf,1); % number of wavenumbers in each scan
        for is = 1:Nscans(idf,1); % each scan...
150         k{idf,is} = flipud(filedata{idf}(1+(is-1)*Nk:is*Nk,kcol));
            S{idf,is} = flipud(filedata{idf}(1+(is-1)*Nk:is*Nk,Scol));
        end % scan loop

    end % data file loop
155

    %% Plot data
    figure(1);
    % subplot(2,1,1);
160 plot(k{1,1},S{1,1});
    xlabel('Wavenumber {\itk} (cm^{-1})');
    ylabel('Raman Signal {\itS} (counts)');
    title('Reference');
    %
165 % subplot(2,1,2);
    % plot(k{1,1},S{1,1});
    % xlabel('Wavenumber {\itk} (cm^{-1})');
    % ylabel('Raman Signal {\itS} (counts)');
    % title('Data');
170
    %% Data Analysis: Estimation Parameters
    windows = [
        % kmin   kmax    Npeaks
    %     -50      50        1
175 %     100     200        1
        450     650        3
    %     675     825        2
        ];
    [Nwin,dum] = size(windows);
180 % GaN Values
    % E2a       144 cm^-1      Window 1
    %
    % A1TO      533 cm^-1      Window 2
```

```matlab
     % E1TO      561 cm^-1
185  % E2b       569 cm^-1
     %
     % A1LO      735 cm^-1      Window 3
     % E1LO      743 cm^-1
     peaks = {
190      % Peak name   kcenter     dkcenter rel. amp.
     %     'Rayleigh'   0          1        0.2
     %     'E2a'        144        3        0.2
         'A1TO'        533.0       5        0.08
         'E1TO'        561.0       5        1
195      'E2b'         569.0       5        1
     %     'A1LO'       735.0      1        0.2
     %     'E1LO'       743.0      1        0.2
         };
     %% Data Analysis: Model-Based Estimation
200  % Algorithm for the data analysis
     %       For each scan...
     %       1. Fit Rayleigh peak and calculate the relative ...
         wavenumber shift,
     %           which is stored as dkappaR
     %       2. Shift the wavenumber component of the data by this ...
         quantity,
205  %           i.e., kappa(i) <- kappa(i) + dkappaR.
     % Nscanstemp = 2;

     for is = 1:Nscans
         currpeaknum = 1; % keeps track of which peak we are tracking
210      for iw = 1:Nwin; % estimate the properties of each window ...
             separately...
             % Extract k and d vectors from each window
             a = min( find( k{is} > windows(iw,1) ) ); % minimum index
             b = max( find( k{is} < windows(iw,2) ) ); % maximum index
             k_w = k{is}(a:b); % windowed k vector
215          d_w = S{is}(a:b); % windowed S vector

             % Estimate the noise in the sample from background data, i...
                .e., the
             % 10 pts near the ends of the window for this peak
             nendpts = 10;
220          bgd = [d_w(1:nendpts);d_w(end-nendpts:end)];
             bgk = [k_w(1:nendpts);k_w(end-nendpts:end)];
             sigmad = std(bgd);
             Rd = 1./sigmad;
             % Also, estimate the background from these points
225          bgline = polyfit(bgk,bgd,1);
             bgslope = bgline(1);
             bgoffset = bgline(2);


             % Quick peak at the data
230          figure(1); % go to figure 1
             plot(k_w,d_w,'-+b',...
```

```matlab
                bgk,bgd,'+g',...
                k_w,k_w*bgslope + bgoffset,'--r');
            drawnow; % force plot update on the screen

            % Estimate the peak values...
            pkidx = floor(mean(find(d_w == max(d_w))));
            pkk = k_w(pkidx); % finds middle of saturated zone
            pkA = max(d_w);

            % Set initial guesses and optimization parameters for each...
                of the
            % peaks
            params = {}; % Clear the params variable
            Npeaks = windows(iw,3);
            for iin = 1:Npeaks
                linename = peaks{currpeaknum,1}; % Name of the line
                k0 = peaks{currpeaknum,2};
                sigmak0 = peaks{currpeaknum,3};
                A0 = pkA*peaks{currpeaknum,4}; % scaled by relative ...
                    amplitude
                params(1+(iin-1)*4:iin*4,:) = {
                    % MIN          MAX        S(1)     S(0)     SIGMAS0 ...
                        NAME
                    0             1e6        A0       A0       Inf      [...
                        linename,'_A']
                    k0-sigmak0  k0+sigmak0  k0       k0       1        [...
                        linename,'_k0']
                    0             100        5        5        0.5      [...
                        linename,'_sigmaG']
                    0             50         1        1        0.5      [...
                        linename,'_sigmaL']
                };
                currpeaknum = currpeaknum + 1;
            end

            sname{is,iw} = params(:,6); % char(sname{1,1}(3,:))
            s1{is,iw} = cell2mat(params(:,3)); % initial guess
            s0{is,iw} = cell2mat(params(:,4)); % a priori estimate
            smin{is,iw} = cell2mat(params(:,1)); % parameter min
            smax{is,iw} = cell2mat(params(:,2)); % parameter max
            Rs0{is,iw} = 1./(cell2mat(params(:,5))); % parameter ...
                covariance
            Ns = length(smin{is,iw}); % number of estimation variables

            % Use LSQNONLIN to do the estimation for us (much cleaner ...
                than the
            % previous methods
            options = optimset(optimset('lsqnonlin'),...
                'display','iter',...
                'TolFun',1e-3,...
                'LevenbergMarquardt','on'); % extra options
                        % 'MaxIter',500,...
```

74

```matlab
275             disp(sprintf('Fitting peak (%g of %g, %3.3g%%)',is,Nscans,...
                    is/Nscans*100));
                [shat{is,iw},resnorm,residual,exitflag,output,lambda,...
                    jacobian] = ...
                    lsqnonlin(@LSQ_obj_func,s1{is,iw},smin{is,iw},smax{is,...
                        iw},options,...
                    @linemodel,Rd,s0{is,iw},Rs0{is,iw},smin{is,iw},smax{is...
                        ,iw},...
                    k_w,d_w,Npeaks,bgoffset,bgslope); % extra parameters ...
                        this line
280         % LSQ_obj_func(s,func,Rdvec,s0,Rs0vec,smin,smax,...
            % k,d,Npeaks,bgoffset,bgslope);
        end
    end % scan loop


285 %%
    % Add to quick plot
    plot(k_w,d_w,'+r',k{is},S{is},'-b'); drawnow;
    %keyboard
    %% Save results
290
    % Put 'em in a file

    % HEADER: Add names of peaks with delimiter to give some reference
    % capability
295 for idf = 1:Ndf
        outfilename = [filename{idf}(1:end-4),'.dat'];
        fid = fopen(outfilename,'w');
        headstr = 'Peak, k0, A, sigma_G, sigma_L, x, y';
        fprintf(fid,'%s \n',headstr);
300     for iis = 1:Nscans
            for iin = 1:Npeaks
                line_name{iis,iin} = peaks{iin,1};
                lineA{iis,iin} = shat{iis}(4*(iin-1)+1);
                linek0{iis,iin} = shat{iis}(4*(iin-1)+2);
305             linesigG{iis,iin} = shat{iis}(4*(iin-1)+3);
                linesigL{iis,iin} = shat{iis}(4*(iin-1)+4);
            end
        end
        for iin = 1:Npeaks
310         for iis = 1:Nscans
                fprintf(fid,'%s, %g, %g, %g, %g, %g, %g \n',...
                    line_name{iis,iin},linek0{iis,iin},lineA{iis,iin},...
                        linesigG{iis,iin},linesigL{iis,iin},x{iis},y{...
                        iis});
                %%%save into structure
    %            test=[line_name{iis,iin},linek0{iis,iin} x{iis} y{iis...
        }];
315         end
        end
        fclose(fid);
    end
```

```matlab
320 %% Wrapup
    endtime = datestr(now);
    % disp(sprintf('Execution time: %g s',toc));
    % disp(sprintf('Program started at %s, ended at %s.',starttime,...
        endtime));
    % profile viewer
325 dbclear all;
    %keyboard
    end % of MAIN


330 %% LEAST SQUARES OBJECTIVE FUNCTION V 2.0
    %~~~~~~~~~~~~~~~~~~~~~~~~~~~~~~~~~~~~~~~~~~~~~~~~~~~~~~~~~~~~~~~~~~~~~~~~~~~~~~~~~~...

    function [fvec,dfds] = LSQ_obj_func(s,func,Rdvec,s0,Rs0vec,smin,...
        smax,...
        k,d,Npeaks,bgoffset,bgslope);
    % Bayesian maximum a posteriori (LSBMAP) vectorized objective ...
        function
335 % This function is the objective for the minimizer used to find ...
        the
    % parameters for the Raman lines that match the provided data.
    %   X - Unknown optimization parameters
    %   K - Wavenumber coordinates
    %   Y - Spectral intensity data
340
    % Input parameters
    %
    % Output parameters
    %   fvec    : vectorized pdf of model with respect to the data
345
    Nd = length(d);
    Ns = length(s);
    fvec = zeros(Ns+Nd,1);
    dfds = zeros(Nd+Ns,Ns);
350
    % M = Misfit function over all data sets
    %   This hold since we assume the experiments are uncorrelated; ...
        the
    %   off-diagonal terms between subsequent experiments are ...
        identically zero.
    [y0,r] = feval(func,s,k,d,Npeaks,bgoffset,bgslope);
355 % linemodel(s,k,d,Npeaks,bgoffset,bgslope);
    fvec(1:Nd,1) = Rdvec.*r;

    % S = Preference function
    Ns = length(s);
360 method = 'pdp';
    switch method
        case 'normprior'
            % Normal (Gaussian) prior
```

```matlab
                    fvec(Nd+1:Nd+Ns,1) = Rs0vec.*(s - s0);
365     case 'pdp'
            % Partially diffuse prior
            for is = 1:Ns
                if (Rs0vec(is) == 0)
                    fvec(Nd+is,1) = 0;
370             else
                    sigmas(is) = 1./Rs0vec(is);
                    C = 1/(smax(is) - smin(is) + sqrt(2*pi)*sigmas(is)...
                        );
                    if s(is) < smin(is)
                        fvec(Nd+is,1) = log(C) - 0.5*((s(is)-smin(is))...
                            ^2)/(sigmas(is)^2);
375                     dfds(Nd+is,is) = -((s(is)-smin(is)))/(sigmas(...
                            is)^2);
                    elseif s(is) > smax(is)
                        fvec(Nd+is,1) = log(C) - 0.5*((s(is)-smax(is))...
                            ^2)/(sigmas(is)^2);
                        dfds(Nd+is,is) = -((s(is)-smax(is)))/(sigmas(...
                            is)^2);
                    else % s on interval (smin,smax)
380                     fvec(Nd+is,1) = log(C);
                        dfds(Nd+is,is) = 0;
                    end
                end
            end
385 end

    if nargout > 1
        for is = 1:Ns
            sp = s;
390         eps_s = 0.0001;
            if sp(is,1) == 0;
                ds = eps;
            else
                ds = eps_s*sp(is,1);
395         end
            sp(is,1) = sp(is,1) + ds;
            [yp,rp] = feval(func,sp,k,d,Npeaks,bgoffset,bgslope);
            dfds(1:Nd,is) = Rdvec.*(yp - y0)/ds;
        end
400 end
    %
    end
    %#################################################################...

    %% Line Model
405 function [y,r] = linemodel(s,k,d,Npeaks,bgoffset,bgslope);
    % This function calculates the intensity profile of an arbitrary ...
        number of
    % peaks (given the parameters S) over the wavenumber range ...
        specified by
```

```matlab
    % K.  The residual (R) is also calculated by this code given the ...
       data
    % vector D.
410
    % Be sure to deal the estimated parameters into the right place
    % s = [
    %          A        % Nth peak amplitude
    %          k0       % Nth peak center
415 %          sigmaG   % Nth peak Gaussian width
    %          sigmaL   % Nth peak Lorentzian width
    %
    %          0        % Baseline slope
    %          0.05*max(ycomp{iis})     % Baseline offset
420 %       ];

    % Superposition of each of the spectral lines...
    for Ni = 1:Npeaks
        A = s(4*(Ni-1)+1);
425     k0 = s(4*(Ni-1)+2);
        sigmaG = s(4*(Ni-1)+3);
        sigmaL = s(4*(Ni-1)+4);

        linei = voigt(k,k0,sigmaG,sigmaL,A);
430     lines(:,Ni) = linei(:);
    end
    % ...and the linear model of the background...
    background = bgslope.*k + bgoffset;
    % ...gives the net intensity distribution
435 y = sum(lines,2) + background(:);

    % Apply a saturation filter to both the data and the Rayleigh line
    satvalue = 70e3; % 75,000 counts
    y( find( y > satvalue ) ) = satvalue;
440 d( find( d > satvalue ) ) = satvalue;

    % Calculate the residual of the model with respect to the theory
    r = ( y - d(:) );

445 % Plot the results
    plot(k,d,'ok',k,y,'-r');
    xlabel('Wavenumber (cm^{-1})');
    ylabel('Intensity (A.U.)');
    pause(0.001);
450
    end

    %% VOIGT FUNCTION AND INTEGRAL
    %-----------------------------------------------------------------------...

455 function f = voigt(omega,omega0,sigmaG,sigmaL,A);
    % This is the "outer" subroutine for the Voigt profile...
    for iw = 1:length(omega)
```

```
                 method = 'approximation';
                 switch method
460                  case 'approximation'
                         % This is the approximation of the Voigt integral from...
                             Puerta and Martin,
                         % 1981, 'Three and four generalized Lorentzian ...
                             approximations for the Voigt
                         % line shape,' Appl. Opt., 20 (22), pp. 3923-3928.
                         p = abs(sigmaL/sigmaG); % must be positive to be in ...
                             upper half-plane.
465                      d = ((omega(iw)-omega0)/sigmaG);
                         z = p + i*d;
                         f(iw) = 2*A*real(cef(i*z,10))/sqrt(pi);
                         % f(iw) = A*real(erfw(z))/sqrt(pi);
                     case 'integral'
470                      omegamax = 2.5*sigmaG;
                         f(iw) = A*quadl(@voigtint,-omegamax,omegamax,[],[],...
                             omega(iw),omega0,sigmaG,sigmaL);
                 end
         end
     end
475 %-----------------------------------------------------------------------...

     % This is the integrand for the Voigt integral if used
     function I = voigtint(omegastar,omega,omega0,sigmaG,sigmaL);
     % I = exp( - ((omegastar - omega0).^2)./(sigmaG.^2) ) ./ ( (...
         omegastar - omega - omega0).^2 + sigmaL.^2  );
     I = exp( - ((omegastar).^2)./(sigmaG.^2) ) ./ ( ( (omega-omega0)...
         - omegastar ).^2 + sigmaL.^2  );
480 end
     %&&&&&&&&&&&&&&&&&&&&&&&&&&&&&&&&&&&&&&&&&&&&&&&&&&&&&&&&&&&&&&&&&&&&&&&&...


     %% CEF (COMPLEX ERROR FUNCTION)
     %----------------------------------------------------------------%...

485 function w = cef(z,N)
     %  Computes the function w(z) = exp(-z^2) erfc(-iz) using a ...
         rational
     %  series with N terms.  It is assumed that Im(z) > 0 or Im(z)...
          = 0.
     %
     %                             Andre Weideman, 1995
490 M = 2*N;  M2 = 2*M;  k = [-M+1:1:M-1]';    % M2 = no. of sampling ...
         points.
     L = sqrt(N/sqrt(2));                       % Optimal choice of L.
     theta = k*pi/M; t = L*tan(theta/2);        % Define variables ...
         theta and t.
     f = exp(-t.^2).*(L^2+t.^2); f = [0; f];    % Function to be ...
         transformed.
     a = real(fft(fftshift(f)))/M2;             % Coefficients of ...
         transform.
```

```
495 a = flipud(a(2:N+1));                        % Reorder coefficients.
    Z = (L+i*z)./(L-i*z); p = polyval(a,Z);      % Polynomial evaluation...
           .
    w = 2*p./(L-i*z).^2+(1/sqrt(pi))./(L-i*z);   % Evaluate w(z).

    %----------------------------------------------------------------------%...

500 end %                            End CEF                              %
    %~~~~~~~~~~~~~~~~~~~~~~~~~~~~~~~~~~~~~~~~~~~~~~~~~~~~~~~~~~~~~~~~~~~~~~~~~%...
```

C.2 Bisquare Fitting Algorithm

Code generated to fit the Raman peak shift as function of stress using a bisquare linear fitting algorithm, in which the outliers do not influence the fit heavily.

Listing C.2: Bisquare Fitting Algorithm. $(\text{Appendix3}/\text{pdp}_f it.m)$

```
    %%%Lt Francisco E. Parada%%%
    %%%Master Thesis%%%
    %%%Phonon Deformation Potential Fitting Code%%%

  5 clear all;clc;pack;

    %%%Young's modulus of GaN and sapphire in GPa%%%
    E_sapphire=452;
    E_GaN=196;
 10
    A=xlsread('strain test results.xls',1,'B22:F30');
    B=xlsread('strain test results.xls',3,'K2:L34');

    %%%Sapphire Data
 15 a=A(:,1).*1e-6.*E_sapphire;
    b_temp=transpose([A(:,4) A(:,5)]);
    b_avg=mean(b_temp);
    b=transpose(b_avg);

 20 %%%GaN Data
    x=B(:,1).*1e-6.*E_GaN;
    y=B(:,2);

    %%%Fitting Options and method
 25 fo = fitoptions('method','LinearLeastSquares','Robust','Bisquare')...
        ;
    ft = fittype('poly1');

    [cf1 gof1]=fit(x,y,ft)
    b_std=std(b)
 30 b_s=sqrt(gof1.sse^2/(length(b)-2))
    [cf2 gof2]=fit(a,b,ft,fo)
```

```
y_std=std(y)
y_s=sqrt(gof2.sse^2/(length(y)-2))
```

Bibliography

1. Beeby, Stephen et al. *MEMS Mechanical Sensors.* Artech House, Inc., Norwood, MA 02062, 2004.

2. Chapra, Steven C. and Raymond P. Canale. *Numerical Methods for Engineers 5th-edition.* McGraw Hill, New York, NY 10020, 2006.

3. Demangeot, F. et al. "Phonon Deformation Potentials in Hexagonal GaN". *Physical Review B*, 69, No 155215:1–5, 2004.

4. Ding, X. et al. "Laser-induced Backside Wet Etching of Sapphire". *Japanese Journal of Applied Physics*, 42, Pt. 2, No. 2B:L176–L178, January 2003.

5. E. Anastassakis, et. al. "Effect of Static Uniaxial Stress on the Raman Spectrum of Silicon". *Solid State Communications*, 88, Nos. 11/22:1053–1058, 1993.

6. Foley, Jason. "Wide Band Gap Materials for "Generation-After-Next" Munitions". Powerpoint Presentation, Dec 2004. AFRL/MN.

7. Foley, Jason. "III-nitride Based Integrated Penetration Fuse and Weapons Effectiveness Sensors for Extreme Environments". Powerpoint Presentation, Sep 2005. AFRL/MN.

8. Hecht, Eugene. *Optics 4th-edition.* Addison Wesley, San Francisco, CA 94111, 2002.

9. Kadleikova, M., J. Breza, and M. Vesely. "Raman Spectra of Synthetic Sapphire". *Microelectronics Journal*, 32:955–958, July 2001.

10. Kuball, M. "Raman Spectroscopy of GaN, AlGaN and AlN for Process and Growth Monitoring/Control". *Surface and Interface Analysis*, 31:987–999, 2001.

11. Liu, L. and J. H. Edgar. "Substrates for Gallium Nitride Epitaxy". *Materials Science and Engineering*, 37:61–127, 2002.

12. Moustakas, T. D. "Growth of III-V Nitrides by Molecular Beam Epitaxy". *Gallium Nitride II*, 33–121. Semiconductors and Semimetals, Academic Press, San Diego, CA 92101, 1999.

13. Muth, J. F. et al. "Absorption coefficient, energy gap, exciton binding energy, and recombination lifetime of GaN obtained from transmission measurements". *Applied Physics Letters*, 71, No. 18:2572–2574, November 1997.

14. Ness, Stanley J. *Stress Analysis of Silicon Carbide Microelectromechanical Systems Using Raman Spectroscopy.* Ph.D. thesis, Graduate School of Engineering, Air Force Institute of Technology (AETC), Wright-Patterson AFB OH, March 2003.

15. Nostrand, J. Van. Email Correspondence, Dec 2005. AFRL/ML.

16. Perlin, P. et al. "Raman Scattering and X-ray Absorption Spectroscopy in Gallium Nitride Under High pressure". *Physical Review B*, 45, No. 1:83–89, January 1992.

17. Smith, Ewen and Geoffrey Dent. *Modern Raman Spectroscopy, A Practical Approach.* John Wiley & sons, West Sussex, PO19 8SQ, England, 2005.

18. Srikar, V. T. and S. Mark Spearing. "Materials Selection in Micromechanical Design: An Application of the Ashby Approach". *Journal of Microelectromechanical Systems*, 12, No 1:3–10, February 2003.

19. Starman, LaVern A. *Characterization of Residual Stress in Microelectromechanical Systems (MEMS) Devices Using Raman Spectroscopy.* Ph.D. thesis, Graduate School of Engineering, Air Force Institute of Technology (AETC), Wright-Patterson AFB OH, April 2002.

20. Zingarelli, John C. *Detection of Residual Stress in SiC MEMS using $\mu - Raman$ Spectroscopy.* Ph.D. thesis, Graduate School of Engineering, Air Force Institute of Technology (AETC), Wright-Patterson AFB OH, March 2005.

REPORT DOCUMENTATION PAGE

Form Approved
OMB No. 0704–0188

1. REPORT DATE *(DD–MM–YYYY)*
23–03–2006

2. REPORT TYPE
Master's Thesis

3. DATES COVERED *(From — To)*
Sept 2005 — Mar 2006

4. TITLE AND SUBTITLE

Characterization of Stress in GaN-on-Sapphire
Microelectromechanical Systems (MEMS) Structures
Using Micro-Raman Spectroscopy

5a. CONTRACT NUMBER

5b. GRANT NUMBER

5c. PROGRAM ELEMENT NUMBER

6. AUTHOR(S)

Francisco E. Parada, 1st Lt, USAF

5d. PROJECT NUMBER

05229, 05338, 06103, 06150

5e. TASK NUMBER

5f. WORK UNIT NUMBER

7. PERFORMING ORGANIZATION NAME(S) AND ADDRESS(ES)

Air Force Institute of Technology
Graduate School of Engineering and Management
2950 Hobson Way
WPAFB OH 45433-7765

8. PERFORMING ORGANIZATION REPORT NUMBER

AFIT/GEO/ENP/06-02

9. SPONSORING / MONITORING AGENCY NAME(S) AND ADDRESS(ES)

Jason Foley
AFRL/MNMF
306 W Eglin Blvd, Bldg 432
Eglin Air Force Base, FL 32542

10. SPONSOR/MONITOR'S ACRONYM(S)

11. SPONSOR/MONITOR'S REPORT NUMBER(S)

12. DISTRIBUTION / AVAILABILITY STATEMENT

Approved for public release; distribution unlimited

13. SUPPLEMENTARY NOTES

14. ABSTRACT

Micro-Raman (μRaman) spectroscopy is an efficient, non-destructive technique widely used to determine the quality of semiconductor materials and microelectromechanical systems. This work characterizes the stress distribution in wurtzite gallium nitride grown on c-plane sapphire substrates by molecular beam epitaxy. This wide bandgap semiconductor material is being considered by the Air Force Research Laboratory for the fabrication of shock-hardened MEMS accelerometers. μRaman spectroscopy is particularly useful for stress characterization because of its ability to measure the spectral shifts in Raman peaks in a material, and correlate those shifts to stress and strain. The spectral peak shift as a function of stress, known as the phonon deformation potential, is determined by applying strain to the material using a four-point strain fixture while simultaneously monitoring the applied strain and recording the Raman spectrum. The deformation potentials are then used to determine stress distribution; the spectral positions of the E_2 Raman mode ($\nu = 569\ cm^{-1}$) in GaN and A_{1g} Raman mode ($\nu = 418\ cm^{-1}$) in sapphire are recorded at each spatial position in a raster map. The μRaman spectroscopy is performed using a Renishaw InVia Raman spectrometer with argon ion ($\lambda = 514.5\ nm$, $h\nu = 2.41 eV$) and helium-neon ($\lambda = 633\ nm$, $h\nu = 1.96\ eV$) excitation sources, and the data is collected across the samples with 5- to 10-μm spatial resolution. Inherent stress and evidence of significant damage in the GaN layer due to MEMS processing is discussed.

15. SUBJECT TERMS

MEMS, μRaman spectroscopy, GaN, residual stress, phonon deformation potential

16. SECURITY CLASSIFICATION OF:

a. REPORT	b. ABSTRACT	c. THIS PAGE
U	U	U

17. LIMITATION OF ABSTRACT
UU

18. NUMBER OF PAGES
102

19a. NAME OF RESPONSIBLE PERSON
Dr. Michael A. Marciniak

19b. TELEPHONE NUMBER *(include area code)*
(937) 255–3636, ext 4529

Standard Form 298 (Rev. 8–98)
Prescribed by ANSI Std. Z39.18